

3D-printable biocompatible, self-adhesive and long-term stable organohydrogel for wearable sensors

Original

3D-printable biocompatible, self-adhesive and long-term stable organohydrogel for wearable sensors / Mogli, Giorgio; Villata, Simona; Chiappone, Annalisa; Frascella, Francesca; Stassi, Stefano. - In: APPLIED MATERIALS TODAY. - ISSN 2352-9407. - 49:(2026). [10.1016/j.apmt.2026.103148]

Availability:

This version is available at: 11583/3009668 since: 2026-04-07T15:02:49Z

Publisher:

Elsevier

Published

DOI:10.1016/j.apmt.2026.103148

Terms of use:

This article is made available under terms and conditions as specified in the corresponding bibliographic description in the repository

Publisher copyright

(Article begins on next page)



3D-printable biocompatible, self-adhesive and long-term stable organohydrogel for wearable sensors

Giorgio Mogli^{a, b}, Simona Villata^a, Annalisa Chiappone^b, Francesca Frascella^a, Stefano Stassi^{a, *}

^a Department of Applied Science and Technology, Politecnico di Torino, C.so Duca degli Abruzzi 24, 10129 Turin, Italy

^b Department of Chemical and Geological Sciences, Università degli studi di Cagliari, Cittadella Universitaria Blocco D, S.S. 554 bivio per Sestu 09042 Monserrato, CA, Italy

ARTICLE INFO

Keywords:

3D printing
Wearable sensors
Ionogel
Polymerizable ionic liquid

ABSTRACT

Hydrogel-based tactile sensors are promising candidates for interfacing soft biological tissues with rigid electronics due to their mechanical compliance and skin-like properties. However, challenges such as limited long-term stability and biocompatibility hinder their broader application. Here, we present a transparent, photopolymerizable, ionically conductive organohydrogel synthesized via a simple one-pot method. The formulation combines a polymerizable cationic monomer, the [2-(methacryloyloxy)ethyl]trimethyl ammonium chloride (METAC), derived from an acrylate choline chloride, with PEGDA as a crosslinker in a binary water/glycerol solvent. METAC serves dual roles as both monomer and ionic conductor, while glycerol forms hydrogen bonds with METAC, enhancing water retention and stability. The resulting material exhibits excellent stretchability (up to 225 %), linear piezoresistive behavior ($GF = 1.54$), and high sensitivity to low compressive pressures (3.35 kPa^{-1} , 0–250 Pa). Moreover, long-term performance is maintained for a remarkable period of 1 year. Biocompatibility was confirmed using a 3D in vitro epidermis model, with no effect on cell viability, morphology or structural proteins. The gel is also compatible with 3D VAT photopolymerization, enabling complex, customizable geometries enhancing stress sensitivity. This versatile, stable, and skin-compatible organohydrogel represents a promising platform for next-generation wearable sensors, soft robotics, and biomedical devices.

1. Introduction

Human skin, the body's largest sensory organ, can simultaneously perceive pressure, strain, temperature, and humidity through a network of specialized mechanoreceptors. Serving as the dynamic interface between humans and their environment, it enables complex sensory feedback essential for perception and control. Inspired by this multifunctionality, recent research has focused on developing artificial electronic skins that replicate and extend the capabilities of natural skin. Flexible, conductive materials capable of transducing diverse environmental stimuli are central to this effort, with promising applications in continuous health monitoring, [1–5] prosthetic feedback, [6,7] and human–machine interfaces [8–12].

In this sensor framework, polymers have gathered great attention since they are more mechanically flexible than commonly used metals [13–15]. Hydrogels, polymers networks able to trap water, specifically emerged as candidate for human-skin imitations, matching skin

mechanical features and providing adaptable electrical properties. Metallic [16,17], carbonaceous fillers [18,19], conductive polymers [20,21] or ions [22,23], are typical ways to endow hydrogels with electrical conductivity, making them suitable for sensors purposes. Ionically conductive hydrogels are among the most versatile options since they are usually transparent, preserving visual information transmission [24,25], and they do not experience reduced stretchability after the addition of fillers [26]. Moreover, there are several ways to introduce mobile ions in the hydrogel water medium by adding salts [27,28], acids [29] or ionic liquids (ILs) [30,31] in the starting formulation.

However, sensors require stability across a wide range of environmental conditions, features that traditional hydrogels cannot provide because of intrinsic water evaporation issues [28,31–33]. Binary solvents systems combining water with and high boiling point organic solvents [34,35] have shown promise in suppressing evaporation while preserving ionic conductivity and flexibility. Alternatively, incorporating ionic liquids into polymer networks provides both solvent and ion

* Corresponding author.

E-mail address: stefano.stassi@polito.it (S. Stassi).

<https://doi.org/10.1016/j.apmt.2026.103148>

Received 17 November 2025; Received in revised form 23 January 2026; Accepted 11 February 2026

Available online 20 February 2026

2352-9407/© 2026 The Author(s). Published by Elsevier Ltd. This is an open access article under the CC BY license (<http://creativecommons.org/licenses/by/4.0/>).

sources [36,37] though solvent leaching can occur; this issue can be mitigated using polymerizable ionic liquids [38,39]. These strategies have led to the emergence of *organohydrogels* [40–43] and *ionogels* [30, 44,45], offering improved durability for soft sensing applications.

Beyond electrical and mechanical performance, assessing biocompatibility is crucial for wearable gel-based sensors that remain in prolonged contact with the skin [9,46]. Wearable sensors are usually tested with simple cells lines grown on 2D monolayers, like dermal fibroblasts [47] or keratinocytes [47,48] or keratinocytes [48], but these *in vitro* models lack the biochemical and mechanical stimuli that regulate cell proliferation, differentiation, and interaction in native tissues [49]. For instance, in 2D culture the natural shape of the cells is lost and the junctions between them does not fully reflect the ones found *in vivo* [50]. This limitation is particularly relevant for skin, a multilayered organ composed of the epidermis, dermis, and hypodermis, each with distinct structures and cell types [51,52]. The epidermis, primarily made of keratinocytes, forms the body's first protective barrier through keratin production and tight intercellular junctions [53]. To mimic such a complex tissue, 3D *in vitro* models have emerged as powerful tools, capturing physiological architecture and function with high reproducibility and relatively low cost [54,55].

Beyond chemical composition and biocompatibility, the fabrication strategy of ionically conductive gels critically influences their performance. 3D printing enables precise control over device architecture, allowing the creation of complex geometries, such as lattices, hollow structures, and auxetic designs, unachievable by conventional methods. These architectures enhance sensitivity and functionality while enabling personalized wearable devices. Among soft-material-compatible approaches, VAT photopolymerization, particularly Digital Light Processing (DLP), offers high resolution, design flexibility, and rapid fabrication. However, stimuli-responsive resins tailored for DLP remain scarce, with only a few reports on 3D-printed ionically conductive strain sensors [56–58]. Developing vat-photopolymerizable, stretchable, and ionically conductive gels thus represents a key challenge and opportunity for next-generation soft electronics.

In this work, we developed a 3D-printable, flexible, and biocompatible strain sensor through a straightforward one-pot synthesis followed by rapid photopolymerization-based fabrication. The precursor solution, composed of a cationic acrylate-functionalized choline chloride monomer in water (METAC), poly(ethylene glycol diacrylate) (PEGDA), and glycerol, enables the formation of a transparent, conductive photopolymerizable organohydrogel. The METAC serves a dual purpose, acting both as an ionic conductor and as part of the polymeric matrix, thanks to the presence of acrylate groups in its structure. Furthermore, glycerol promotes the stability of the gel over time by preventing water evaporation preserving both its mechanical and sensing properties for over 1 year. The developed organohydrogel exhibits excellent stretchability (over 225 %), with a linear piezoresistive response ($GF = 1.54$) and low hysteresis. Its low compressive Young's modulus (3.18 kPa) facilitates seamless mechanical integration with biological tissues and provides high sensitivity to small pressures (3.35 kPa^{-1}). Additional features important for wearable applications include self-adhesion and linear sensitivity to ambient humidity (1.305 %/RH). Biocompatibility was evaluated via direct contact with a 3D *in vitro* model of human epidermis. The results were promising since no tissue impairment was observed, and key epidermal markers such as cytokeratin and filaggrin, proteins critical for human keratinocyte function [59], were preserved. By incorporating a commercial dye into the photopolymerizable formulation, we successfully fabricated high-resolution 3D architectures using DLP technology, enhancing the sensor's ability to detect mechanical deformation. This flexible conductive gel combines long-term stability, multi-stimuli responsiveness, and scalable fabrication, presenting a highly promising platform for next-generation wearable electronics and skin-integrated devices.

2. Results

2.1. Material optimization and electromechanical characterization

The METAC aqueous solution represents a promising material for developing soft, conductive gels due to its ability to undergo radical polymerization, retain water, and maintain biocompatibility [60]. METAC is composed of an acrylate modification of choline chloride, forming with water a liquid monomer that exhibits ionic liquid features that inherently support ionic conductivity. This is due to its structure, which includes a positively charged quaternary ammonium group fixed on its backbone and a mobile chloride ion (Cl^-), which remains active in the water-rich environment, enabling electrical conductivity (Fig. 1a). In addition, the presence of a carbon–carbon double bond in METAC's structure enables photopolymerization in the presence of a suitable photoinitiator, as already documented in literature [61]. Unlike standard choline chloride or other ionic liquids, METAC can simultaneously serve as both the monomer for forming the polymeric matrix and as the source of ionic conductivity. This dual function marks a significant advantage compared to traditional ionogels, where the ionic liquid typically acts as a solvent within a polymeric host matrix, incurring the potential leaching of the solvent. Similarly to other polymerizable ionic liquids (PILs), METAC serves as an intrinsically ionic monomer, forming a polymer network that can be used in strain sensors; however, most reported PILs for such applications are imidazolium-based [37]. These ionic liquids usually exhibit environmental and human safety concerns due to limited biodegradability, cytotoxicity [62] water ecotoxicity [63]. In contrast, choline chloride-based monomers present great advantages on these latter in terms of environmental impact and biocompatibility [64,65]. In the present case, METAC-based samples can be fabricated through a rapid, efficient, solvent-free, and room-temperature process [66]. Indeed, a straightforward one-pot approach was employed to formulate the ionogel precursors. The crosslinker PEGDA and the water-soluble, UV-sensitive photoinitiator lithium phenyl-2,4,6-trimethylbenzoylphosphinate (LAP) were directly dissolved in the METAC aqueous solution. Although the resulting material can be formally classified as a hydrogel from the solvent perspective, since water constitutes the liquid phase, it exhibits enhanced properties beyond those of conventional hydrogels, owing to the multifunctional role of METAC in both network formation and ionic conductivity. Four different PEGDA concentrations were investigated: 0 wt%, 1 wt%, 2wt% and 5 wt% (METAC_0, METAC_1, METAC_2, METAC_5) with respect to METAC solution. Thanks to its two acrylate groups, PEGDA can covalently crosslinks METAC chains. To evaluate reactivity to UV light, all formulations were tested through photorheology. Samples gel points, defined as the time in which storage and loss moduli intersect, occur approximately 20 seconds after the light is turned on for all formulations (Figure S1a-d). Moreover, observing the storage moduli of samples after photopolymerization, it is clear that, as the PEGDA concentration increased, the stiffness of the obtained hydrogel grew due to the higher number of crosslinks between poly (METAC) chains (Fig. 1b). Surprisingly, sample METAC_0, produced without the addition of the crosslinker, shows reactivity and a final G' modulus similar to sample METAC_2 and even higher than METAC_1. This behaviour can be attributed to the strong interchain ionic interactions of poly(METAC) that can impart rigidity to the linear polymer. The addition of PEGDA has then a dual effect: on one side it increases the crosslinking density leading to a stable and rigid covalent network after Figure polymerization but, on the other side it can decrease the ionic interactions. The first effect is predominant only when more than 2wt% of PEGDA is used.

Water-evaporation remains the greatest challenge to overcome in hydrogel applications. METAC starting solutions contains only 25 % of water in weight, but as showed later in this work, evaporation issue will modify the mechanical and electrical properties of the prepared material. Therefore, water should be at least partially replaced with a low-

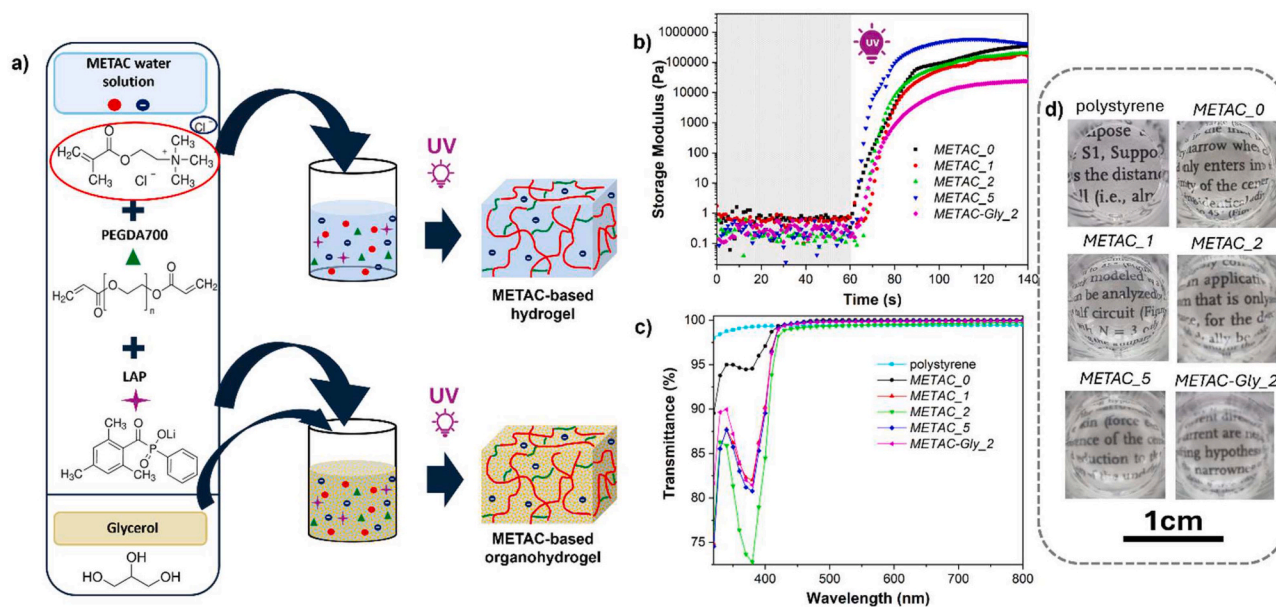


Fig. 1. (a) Chemical composition of METAC gels: on the right the scheme of the hydrogel (up) and organohydrogel (down) formation. (b) Storage moduli of the different kinds of photopolymerizable formulations tested with real time photorheologies. UV light was turned on at 60 seconds. (c) UV-vis transmittance spectra of the different METAC formulations compared with polystyrene film. (d) Photographs of different polymerized METAC hydrogel/organohydrogel samples showing their transparency in the visible optical range.

volatility solvent. Here, glycerol was directly dissolved in METAC water solution leading to the formation of an organohydrogel (Fig. 1a). Indeed, glycerol is known to improve the long-term mechanical and electrical stability of hydrogels thanks to the ability to form hydrogen bonds with water free molecules due to the high density of hydroxyl groups in its structure (ATR analysis are reported in Figure S2). This hinders water crystallization, as well as water evaporation [41,67,68]. Furthermore, in the present case, glycerol can also form strong interactions with the choline chloride ions [69] leading to the formation of a complex system based on secondary bonds which increases the material stability. Thanks to its hydrophilic nature, it did not affect the one-pot formulation preparation and its reactivity to UV light (Figure S1e) and helped in retaining water in the photopolymerized material. In that study, a METAC gel containing 50 wt% of glycerol and crosslinked with 2 wt% of PEGDA relative to the METAC water solution, was successfully prepared and named as METAC-Gly 2. As shown by storage modulus after photopolymerization (Fig. 1b), glycerol presence decreased storage modulus. This effect results from the lower polymer chains density than in the hydrogels, as the METAC is dissolved in a larger volume of water/glycerol solvent. Moreover, the addition of this amount of glycerol enabled the increasing of viscosity to higher values (Figure S1f), without significantly affecting the reactivity. This enables the implementation of DLP photopolymerization techniques which typically requires low to moderate viscous inks ($< 10 \text{ Pa}\cdot\text{s}$) with good reactivity (tens of seconds) compatible with DLP technology [28,70,71]. Although METAC gels are formally classified as hydrogels due to their aqueous solvent, the incorporation of glycerol imparts organohydrogel-like behavior, characteristic of binary solvent systems composed of water and polyol [72]. The dense network of hydrogen bonds formed between poly(METAC) chains and glycerol molecules enhances both the mechanical robustness and electrical stability of the gel over time. Moreover, this interaction effectively suppresses water evaporation, contributing to the long-term reliability of the material's sensing performance. Therefore, in this work, to emphasize the nature of the solvent phase, the METAC samples are referred to as hydrogels and METAC-Gly ones as organohydrogels reflecting the presence of water alone or a binary water-glycerol solvent system, respectively

High transparency in the visible range (approximately 400 nm-700

nm) represents a great property for wearable sensor, to be able to monitor skin conditions underneath in a minimally visible way [73–75], but also for other electronic applications such as stretchable touch screen [76]. The transmittance spectrum of the METAC-based gels and METAC-Gly_2 gel showed optical transparency for wavelengths above 450 nm (i.e. transmittance % ≥ 95 %) (Fig. 1c), comparable to the properties of transparent polystyrene film. Images showing the transparency of the prepared material when placed over a book page are reported in Fig. 1d.

Stretchable dumbbell-shaped sensors were easily obtained by pouring in PDMS molds the formulations and exposing them to UV light. Copper strips were used as electrodes. The gel samples were subjected to tensile test (Fig. 2a), showing all an optimal stretchability above 130 % of strain. In particular, the hydrogel samples with no crosslinks or a low amount of them (METAC_0, METAC_1, METAC_2) displayed a higher elongation at break up to 325 %. This may be due to the few or absent crosslinking points between METAC chains, that can be easily extended without undergoing rupture. By increasing the PEGDA concentration and thus the crosslinking density, as in the METAC_5 samples, stiffer hydrogels are obtained, that exhibit lower stretchability [77,78]. The effect of crosslinker was further evaluated on the corresponding organohydrogel, analysing the same PEGDA concentrations (0,1,2,5 %). Organohydrogel samples without crosslinker (0 wt %, METAC-Gly_0) were not self-standing. The high solvent content (50 wt% glycerol with respect to the METAC solution, in addition to the water associated with METAC) prevented effective curing of the matrix, resulting in a highly sticky material unable to maintain a stable shape (Figure S3a). The organohydrogels samples were able to sustain 200 % strains without rupture (Fig. 2b). Also in this case, the stiffness of organohydrogels increased with increasing crosslinker concentration. However, samples containing 5wt% of PEGDA displayed an elastic modulus comparable to that of samples with 2wt % of PEGDA, suggesting that beyond 2 % the additional crosslinker does not effectively increase the interchain crosslinks in presence of glycerol. In any case, all formulations were able to withstand deformations well above the strain range involved in human motion (0–55 %) [79], with elastic moduli below 100 kPa for the organohydrogel samples (Fig. 2c). The organohydrogels' lower stiffness, resulting from the reduced polymeric content compared to the

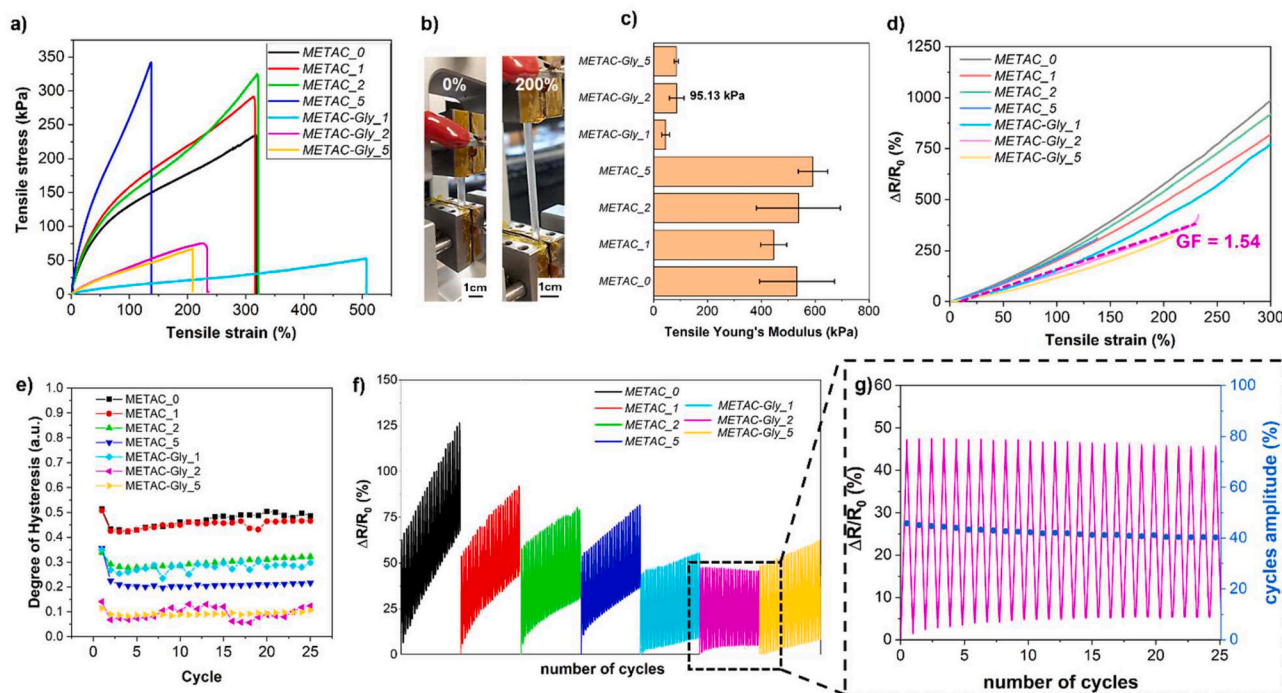


Fig. 2. (a) Tensile stress-strain curves up to rupture for gel-based dumbbell-shaped samples (b) Images of a METAC-Gly₂ sample at rest (left) and subjected to 200 % of tensile strain (right). (c) Tensile Young's modulus for the various kinds of samples. 5 independent samples were tested for each formulation. (d) Piezoresistive responses to external tensile strains for hydrogel and organohydrogel samples. Linear fitting of METAC-Gly₂ organohydrogel curve is reported with the dashed pink line ($R^2=0.995$). On the bottom right the gauge factor is reported (e) Degree of mechanical hysteresis of the hydrogel/organohydrogel samples for all the 25 cycles. (f) Tensile cyclic test for METAC gel samples. 25 cycles of loading and unloading were performed. The curves are horizontally offset to improve clarity. (g) Zoom of the cyclic test for METAC-Gly₂ gel specimen. The blue circles represent the resistance cycles amplitude and are referred to the right scale.

corresponding hydrogels, is closer to that of soft tissues [80], making them more suitable for human-related applications

Tensile tests were then coupled with electrical resistance measure to evaluate the strain sensing properties of the materials. Since METAC based gels were ionically conductive, stretching them increases the migration path for dissolved ions, leading to conductivity decrease, and thus an increase in electrical resistance. Therefore, external deformations could be detected by checking the resistance variation. This is the basic concept of the positive piezoresistive transduction methods [81]. In Fig. 2d the relative resistance variations, computed as reported in Eq. 3, with respect to the strains applied of METAC based samples are reported. All the hydrogels displayed a similar piezoresistive behaviour. The resistance variations under applied strains of the corresponding organohydrogels are slightly lower. This may be due to the glycerol presence that makes the transport medium for ions more viscous, as reported previously in the rheology test (Figure S1f), hindering their response to external deformations [82,83]. Indeed, conductivity of METAC-Gly₂ was nearly half of that of the METAC₂ hydrogel, decreasing from 0.28 S/m to approximately 0.11 S/m (Figure S3b). In addition, the electrical conductivity was not significantly affected by variations in crosslinker concentration. However, the organohydrogels displayed a greater linearity of the piezoresistive transfer curve (Figure S3c), with comparable gauge factors in the 0-55 % strain range (Figure S3d). As a representative case the METAC-Gly₂ samples exhibited a gauge factor of 1.54 within its whole strain range (Fig. 2d).

Repetitive loading and unloading tensile strains were applied to the hydrogel and organohydrogel samples to investigate the hysteresis in sensing response. Low hysteresis is a critical factor in sensor development, as it indicates that the sensor measurements are repeatable [84]. Mechanically, the METAC hydrogel specimens showed a higher hysteresis with respect to the organohydrogels samples when stretched cyclically up to 50 % of their initial length (Figure S4a). This is a result of the viscoelastic nature of polymeric networks. METAC polymeric chains

sliding under mechanical deformation causes the irreversibility of hydrogels. When covalent crosslinking density increases, hysteresis decreased due to the greater number of anchoring points among the chains, as confirmed by the degree of hysteresis (DH) reported in Figure S4b. However, rupture of the covalent crosslinking points leads to irreversible residual strain. In particular, the role of glycerol is likely related to the increased number of reversible physical bonds, mainly the multiple hydrogen bonds enabled by glycerol hydroxyl groups, which facilitate an improved mechanical recovery [85,86]. Moreover, the reduced hysteresis might be attributed to the glycerol effect as plasticizer which improves the intermolecular chains flexibility, reducing their interactions and therefore facilitating the structural recovering after deformation [41,87]. The combined effect of glycerol and increased crosslinking concentration results in a low average DH, of approximately 9 %, for METAC-Gly₂ and METAC-Gly₅ samples (Figure S4b). This behaviour is also reflected from the electrical point of view. An increasing residual resistance after each tensile cycle is present in all the hydrogels, while in the organohydrogels this drift is substantially lower, in particular for METAC-Gly₂ sample (Fig. 3a). Moreover, cycles amplitude among subsequent cycles is quite stable for METAC-Gly₂ specimen, a sign that sensitivity drift is almost null for repetitive loading-unloading stimuli (Fig. 3b). Due to its similar electrical and mechanical properties with other organohydrogels, combined with slightly higher sensitivity, the organohydrogel containing 2 wt % PEGDA (METAC-Gly₂) was considered for further in-depth investigation.

Considering its optimal mechanical and piezoresistive sensing properties, together with several additional features described in the subsequent sections, including adhesiveness, long-term durability, skin compatibility, humidity sensitivity, and 3D customizability, the METAC-Gly₂ organohydrogel displayed strong competitiveness among reported gels with mixed or non-aqueous liquid phases (Table S1). In addition, compared with other reported METAC-based gels [88–90], this

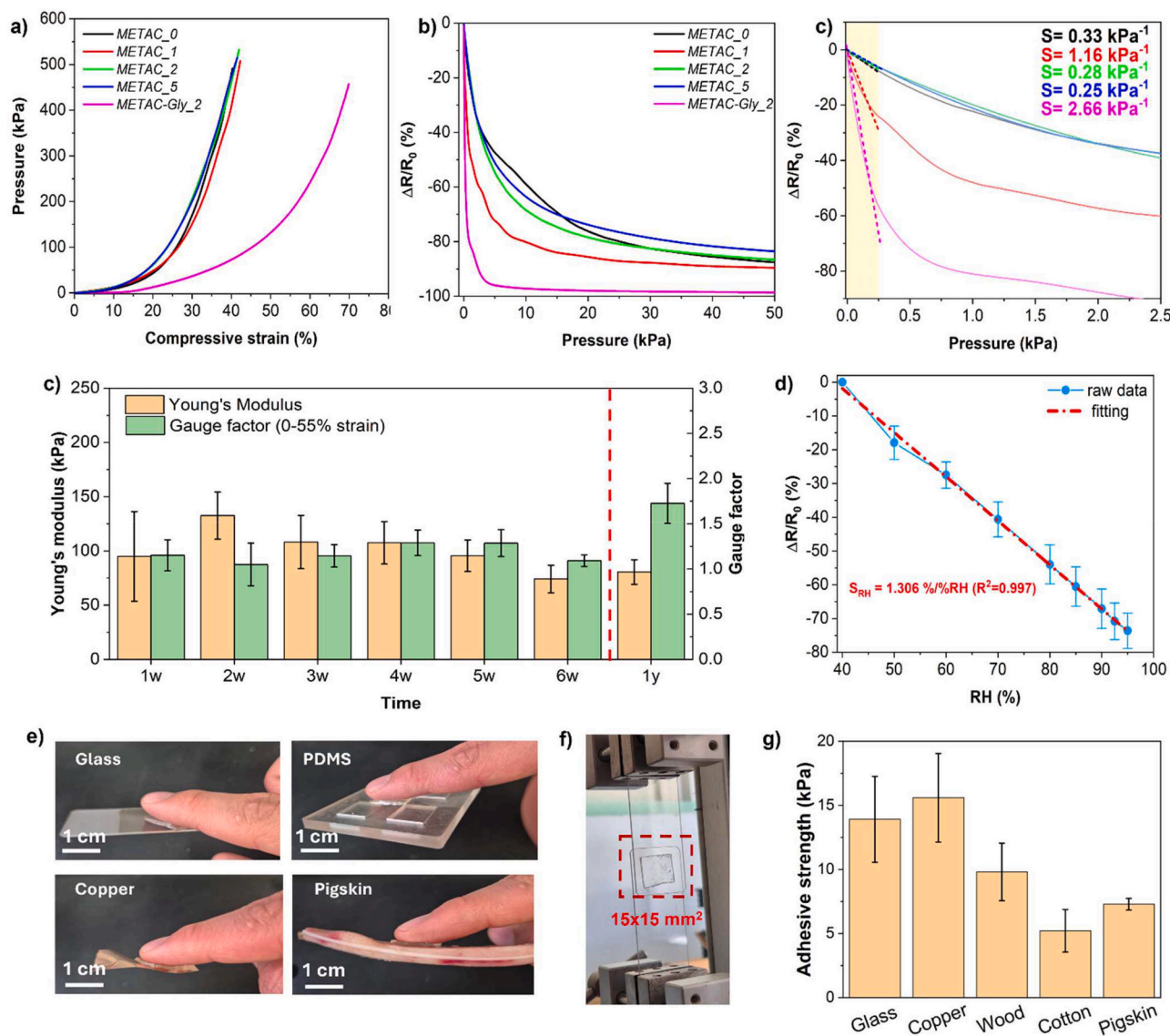


Fig. 3. (a) Compressive tensile stress-strain curves up to 50N for parallelepiped-shaped gel samples ($10 \times 10 \times 1.5 \text{ mm}^3$). (b) Piezoresistive response to applied pressures for gel samples. The area highlighted by black dashed rectangle is zoomed in the next figure. (c) Zoom-in at low pressures of piezoresistive curves. The dashed lines are the linear fits between 0 and 2.5 kPa; on the top right, the pressure sensitivities are reported. R-squared are 0.991, 0.969, 0.971, 0.999, 0.983 for METAC_0, METAC_1, METAC_2, METAC_5, METAC-Gly_2, respectively. (d) Long-term stability of *METAC-Gly_2* organohydrogel samples, subjected to tensile test up to 55 % of strain for 5 subsequent weeks. The same samples were tested also after 1 year-period. Young's modulus (orange bars) is referred to the left scale, Gauge factor (green bars) is referred to the right scale. Standard deviations are referred to an independent pool of 5 samples. (e) Resistance variations of *METAC-Gly_2* organohydrogel samples related to humidity changes. The light blue area evidences the standard deviations referred to 4 independent specimens. The red dash-dot line highlights the linear fitting of the raw data. The corresponding slope (sensitivity) is reported in red on the lower part of the figure. (f) The *METAC-Gly_2* organohydrogel adhered to several substrates. (g) Scheme of the setup for the adhesion test. (h) Picture of the setup of the adhesion test. (i) Adhesive strength of *METAC-Gly_2* organohydrogel to several substrates. Five independent samples were tested.

organohydrogel can be fabricated via a simple one-pot process without copolymerizing METAC with additional monomers, which significantly simplifies the synthesis and enhances its practical appeal.

Parallelepiped-shaped hydrogel/organohydrogel samples were then subjected to compression tests to evaluate their responsiveness to pressure loads. The *METAC-Gly_2* samples resulted more deformable to applied pressures as can be seen from Fig. 3a where the specimen reached a compressive strain of 65% when a load of 50 N is applied. This results in softer materials (Figure S4c). In particular, the *METAC-Gly_2* gels displayed the lowest compressive and tensile Young's moduli, equal to 3.18 kPa and 95.13 kPa respectively. These values are of the same order of magnitude as those found in living tissues [91,92], demonstrating that this material offers superior mechanical compliance for applications related to the human body. The compressive tests were

coupled with electrical measures, finding the piezoresistive behaviour of METAC based samples with respect to the applied pressures. In this case, since the specimens are compressed and the distance between the electrodes diminished, the ionic conductivity increases, leading to the electrical resistance decrease (Fig. 2f). All the specimens showed a great responsiveness to pressures up to 2.5 kPa. In particular, between 0 and 250 Pa a quasi-linear dependency within pressure and resistance variations is visible (Fig. 2g). In this range, the *METAC-Gly_2* specimens displayed an outstanding average sensitivity of 3.35 kPa^{-1} , more than three times the value of other hydrogels (figure S4d). Since the electrical resistance strongly depends on electrodes distance, the *METAC-Gly_2* gel samples, exhibited the greatest deformability among the studied materials under the same applied force, resulting in higher resistance variations at maximum compressive stress.

Moreover, glycerol presence effectively improved the long-term stability of both electrical and mechanical features of the flexible sensor. In Figure S5a,b the percentage variations of tensile Young's modulus and gauge factor with respect to their values of the freshly prepared *METAC-Gly_2* organohydrogel and the corresponding hydrogel (*METAC-2*) samples, are reported within a 4-week period in which they were stored at room temperature in open air conditions. Stiffness of *METAC_2* samples underwent a substantial growth already after 1 week, evidence that the water within the polymeric network had started evaporating. Then, after 1 month, Young's modulus increased by roughly 80 times. On the other hand, *METAC-Gly_2* demonstrated a better stability beyond 1 month of testing. The tensile Young's modulus and the tensile strain sensitivity values remain around 100 kPa and around 1.2, respectively, throughout the entire period of 5 weeks (Fig. 3c). This proves the role of glycerol in reducing water evaporation by bonding free water molecules, thanks to the abundance of hydroxyl groups on its backbone. This is also evident from conductivity measures. The as-prepared *METAC-Gly_2* samples exhibited lower conductivity compared to the *METAC_2* ones due to the higher viscosity of the ions transport medium caused by the presence of glycerol. However, after few weeks, the water-based samples showed a decrease in conductivity related to water evaporation, while *METAC-Gly_2* samples maintained a stable conductivity trend over the 4 weeks period (Figure S5c). Moreover, the same *METAC-Gly_2* samples were tested 1 year after the initial measures. Remarkably, they displayed an almost unvaried elastic modulus and a slightly increased sensitivity (Fig. 3c). Although the tensile tests were performed in a room without humidity and temperature control, the gauge factor increase may be attributed to the rising ionic concentration and consequently, increased conductivity (Figure S5c), derived from copper electrodes oxidation, as evidenced by the bluish-green appearance 1-year-old sample displayed in Figure S5d. However, these samples remain potentially functional after one year, as also visually confirmed by their optimal stretchability (Figure S5e). The lower stiffness, the enhanced long-term stability and the reduced hysteresis makes the *METAC-Gly_2* sensors a preferable choice for flexible sensors applications.

In addition, *METAC-Gly_2* organohydrogel sensors showed an optimal sensitivity to humidity variations. Glycerol can naturally absorb atmospheric water molecules [93] leading to a decreased viscosity of the ions transport medium and thus to a facilitated ions mobility. Therefore, when exposed to a water vapour-rich atmosphere, sensor resistance decreased. *METAC-Gly_2* specimens were exposed in closed environments with different relative humidity levels while their resistance was monitored for each humidity step. The organohydrogel showed a quasi-linear dependency between resistance variations and changes in relative humidity (Fig. 3d) with a sensitivity of 1.306 %/%RH.

The exceptional conformability of the *METAC-Gly_2* specimens, which ensure high surface area in contact with the application surfaces, combined with the high density of functional groups capable of forming reversible bonds, such as -OH groups, and electrostatic interactions arising from the positively charged polymeric chains, contributes to their strong self-adhesion to different substrates [61,94,95]. This is clearly visible by the pictures in Fig. 3e, where the freshly made *METAC-Gly_2* organohydrogel readily adhered to several materials, such as glass, polydimethylsiloxane (PDMS), copper and pigskin. Pull off test were then conducted to quantify the adhesive strength of this gel. As made rectangular specimens of the material were placed between the substrates (Fig. 3f) and then subjected to the tensile test to evaluate gel adhesive strength. The force at which the detachment starts, namely the peak force in the force-displacement graph (Figure S6a) was divided by the contact surface to compute the adhesive strength (Fig. 3g). The *METAC-Gly_2* specimens adhered to glass, copper, wood, cotton, and pigskin substrates with strengths of 13.9 kPa, 15.5 kPa, 9.8 kPa, 5.2 kPa, and 7.3 kPa, respectively. Although the measured adhesion values were lower than those of the strong double-sided tape (VHB tape, 3M, ≈ 77 kPa on glass, Figure S6b), this physical adhesiveness was still sufficient

to ensure effective adhesion to the various materials without the need for additional tape and without causing skin irritation that a stronger adhesive will cause upon removal, in case of wearable applications, as also reported in literature [9,96–99]. The good self-adhesion property is confirmed by the application of both the casted samples and the samples fabricated, as described later, via 3D printing, to the volunteer's bare finger. The samples adhered firmly and conformed well to the skin, following finger movements and leaving no residuals upon peeling (Supporting Movie 1 and 2).

2.2. Biocompatibility test

This direct contact with the skin also highlights the importance of assessing the materials' cytotoxicity. Wearables, one of the major application fields of flexible sensors, require the direct contact between the sensitive materials and the human skin. To have a first indication on possible cytotoxic effects of the METAC and PEGDA matrix used in the *METAC-Gly_2* organohydrogel, the effects of conditioned medium on the viability of human keratinocytes (HaCaT) was investigated. This cytotoxicity tests were performed to identify any possible toxic release of compounds from the sensor. The proliferation trends were promising, with no cytotoxic effects observed after 24 hours (Figure S7). While proliferation in the conditioned medium was lower than in the treated control after 72 h, there was still significant growth from 24 to 72 h. However, conventional 2D *in vitro* testing typically fail to replicate the complexity of the biological system where the sensors will be applied. Therefore, considering the effects of flexible materials on 3D epidermis *in vitro* models could provide a more in-depth analysis of their toxicity. Indeed, while 2D cultures consist of a single layer of cells on a flat surface, the 3D model replicates the physiological layered structure and barrier function of real human skin. This makes it possible to assess how substances released from the sensor might penetrate the skin and cause irritation, cytotoxicity or damage under realistic conditions. The 3D model provides more accurate data on tissue viability and potential skin toxicity, which 2D cultures cannot capture due to their lack of structural complexity and physiological relevance. To evaluate the epidermal compatibility with the flexible sensors, 5 weeks-old epidermis samples were analysed through immunofluorescence after the contact with the sensors for 1h, 6h and 24h, as explained in the scheme in Figure S8. This test was conducted for the METAC and PEGDA polymeric matrix, namely the *METAC_2* hydrogel (Figure S9), the casted *METAC-Gly_2* organohydrogel (Figure S10) and the 3D printed *METAC-Gly_2* organohydrogel with the addition of commercial dye (tartrazine) (Fig. 4), which was necessary to achieve good printing resolution, as explained later. The epidermis model built by the human keratinocytes (i.e. the main cell type constituting the epidermal layer *in vivo*) showed great vitality and physiological cell morphology after all the incubation timepoints (Fig. 4 and S8,9). To pursue these information, cellular cytoskeleton was marked with phalloidin, cellular nuclei with DAPI and cells were also stained with epidermal markers, i.e. pancytokeratin and filaggrin, both of which involved in the structure of an organized, stable, and functional barrier that can be impaired by the contact with damaging materials.

Specifically, cytokeratins are a group of proteins that constitute intermediate filaments, primary cytoskeletal components that provides structural support to keratinocytes [100]. As expected, in healthy keratinocytes, their expression, detected by pancytokeratin antibody, was found both in the bare sample (Fig. 4a or S8,9a) and in the samples that hosted the sensors (Fig. 4b-d or S8,9b-d), confirming the survival and the grown of the upper layer of the model. Then, the focus moved on filaggrin, a structural protein mainly found in the outermost layer of the epidermis, known as the stratum corneum (SC). It is responsible for generating natural moisturizing factors that contribute to barrier functions by protecting skin against microbial colonization, and for assembling keratin filaments, leading to the creation of a network that leads to the transformation of keratinocytes into flattened corneocytes [101].

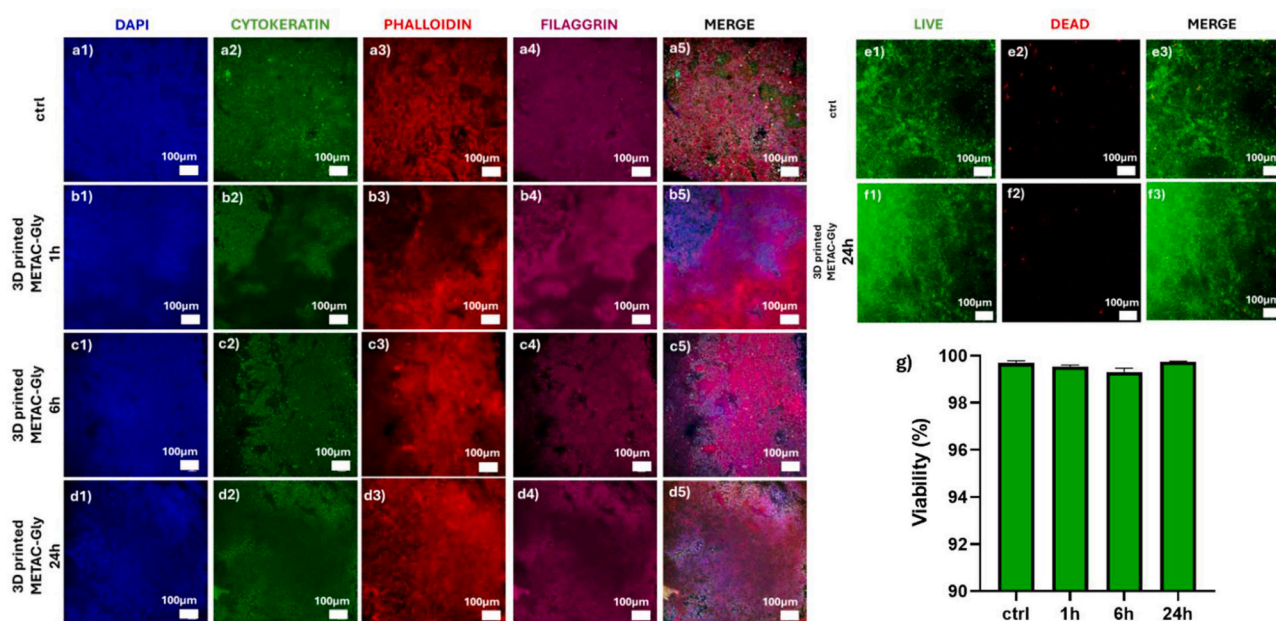


Fig. 4. Immunofluorescence images of 3D *in vitro* epidermis model in contact with 3D printed sensors of *METAC-Gly_2* with tartrazine for 1h (b), 6h (c) and 24h (d), respect to the control (a). DAPI was used to stain cellular nuclei, TRITC-Phalloidin was used to stain the cytoskeletons, pancytokeratin is visualizable in FITC while in Cy5 it is possible to observe filaggrin. Images are at 20x magnification. e) and f) Fluorescent images of LIVE/DEAD assays on 3D *in vitro* epidermis model in contact with 3D printed sensors of *METAC-Gly_2* with tartrazine, for 24h (f), respect to the control (e). The green channel shows alive cells while the red channel shows dead cells. Images are at 20x magnification. g) Quantification of cells viability starting from LIVE/DEAD analysis.

Again, filaggrin was found both in the bare sample (Fig. 4a or S8,9a) and in the samples that hosted the sensors at all the studied time points (Fig. 4b-d or S8,9b-d). This means that the materials did not induce damage both in the cellular shape and in these proteins' presence, promoting them to optimal candidates for topical and wearable sensors. To further investigate the compatibility of the printed formulation (i.e. *METAC-Gly_2* organohydrogel with the addition of tartrazine), epidermis samples were analysed using LIVE/DEAD kit at 1, 6 and 24 h after contact with sensor (Figure S8, showing all the contact timepoints). As can be evaluated both from the resulting images in Fig. 4e,f and Figure S8a-d and in the quantification reported in Fig. 4g, the epidermal exposure to the 3D printed sensors did not affect the keratinocytes viability, that was for all the timepoints >98%. This indicates that these materials do not cause a remarkable loss in epidermis viability, putting them in a prominent position for wearable and topical applications.

2.3. 3D P

2.3.1. Rinted flexible tactile sensor

In addition to skin compatibility, their processability is another key feature to consider for enhancing the practical application of soft sensors. In this context, additive manufacturing is emerging as a crucial fabrication method in the field of soft sensors, due to the rapid processing, enhanced repeatability and ability to create personalized geometries. Since the *METAC-Gly_2* is a photopolymerizable mixture, VAT photopolymerization techniques can replace the traditional casting approach followed by UV exposure. Here DLP printer was used to fabricate complex 3D shapes. The addition of a widely used, food-grade commercial colorant (tartrazine) [102], to the precursor formulation was necessary to improve printing resolution by limiting the UV light scattering, as shown by Figure S11a. Tartrazine resulted effective, as the 3D-printing wavelength lies within the tail of its main absorbance peak (~430 nm) [103]. The effective reactivity of the formulation with the addition of tartrazine was confirmed by the gel point reported in figure S11b. The cured gel reported mechanical properties comparable to the ones of the organohydrogel without dye as evidenced by the similar storage moduli after the photo-curing process in Figure S11c. Moreover,

conductivity and adhesivity 3D printed of *METAC-Gly_2* samples with tartrazine remained almost unchanged compared to the neat casted samples (Figure S11d,e and Movie 2).

Afterwards, geometries designed to enhance force sensitivity were printed. *Strip*, *classic mesh* with a perpendicular pattern and *re-entrant mesh* geometries were investigated as tensile force sensors (Fig. 5a) while *bulk*, *gyroid*, *honeycomb lattice (HC lattice)* architectures were explored as pressure sensors (Fig. 5b). Tensile sensors were tested up to 100% strain. 3D printed *strip* samples of the same dimensions were used as control. As shown in Figure S12a, the two meshes exhibited a lower stiffness, due to the high number of voids in their structure. The *re-entrant mesh* exhibited a Young's modulus that was about the 30% the one of the *strip*, indeed (Figure S12b). Moreover, both the meshes were able to withstand 100% of deformation without breaking (Figure S12c). The electrical resistance variation was measured during the test and showed that the softer is the sensor, the higher its resistance variations following the applied tensile force (Fig. 5c). Under the same applied force, sensors with voids exhibited a greater deformation than the *strip* sensor. This is reflected by higher resistance changes indicating a greater sensitivity to the applied stresses. Two distinct linear ranges (R1, R2) of the resistance response can be highlighted for each examined architecture (Fig. 5c). The *strip* sensors displayed good linearity between 0 and 10 kPa and between 15 and 30 kPa. The *classic mesh* was approximately linear between 0 and 7.5 kPa and 10-20 kPa, while the *re-entrant mesh* showed linearity between 0-2.5 kPa and between 4- 7.5 kPa. All the R-squared were above to 0.96 (table in Fig. 2). The *re-entrant* geometry enhanced the sensitivity to tensile stress below 2.5 kPa by a factor 4 with respect to the *strip* sensors. In addition, between 4 and 7.5 kPa it reached a sensitivity of 0.47 kPa^{-1} , the highest value observed in the stress ranges studied. The *classic mesh* exhibited a broader stress range, with a sensitivity lower than the one of the *re-entrant* but higher than that of the bulky samples (Fig. 5d). Average sensitivity values are also reported in the table in Figure S12d.

A similar behaviour was observed in 3D printed samples designed for compressive pressure sensing. *Gyroid* and *honeycomb lattice (HC lattice)* architectures were printed with an optimal resolution and tested under compression test comparing their sensing performance with *bulk* sample

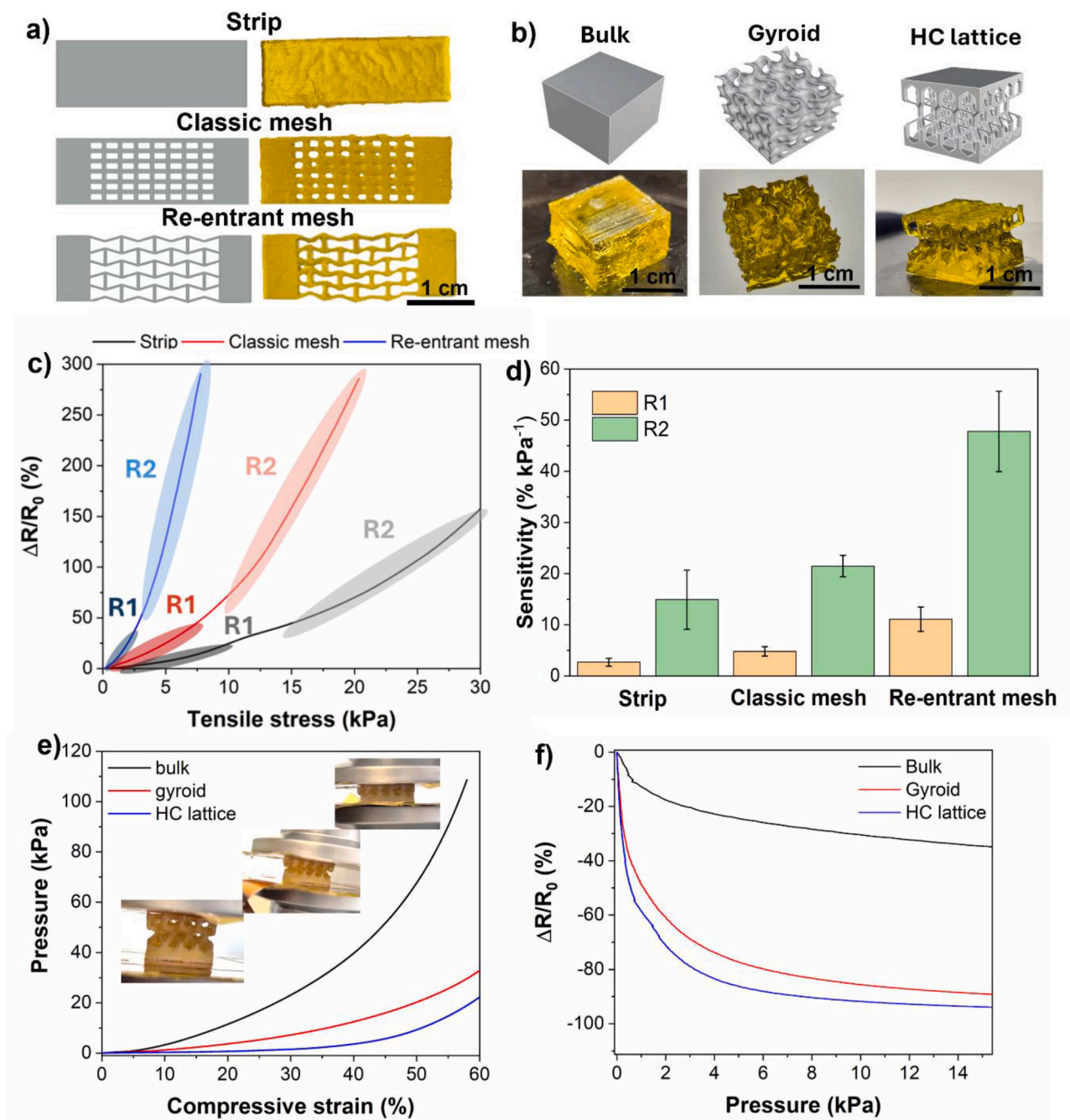


Fig. 5. (a) 3D printed *METAC-Gly₂* architectures for tensile force sensing and their corresponding STL models. b) 3D printed *METAC-Gly₂* architectures for pressure loads sensing and their corresponding STL models. c) Electrical resistance variation under tensile loading for *strip*, *classic mesh* and *re-entrant mesh* 3D printed samples. The first linear region (R1) is highlighted in the dark-coloured ellipses. The second linear area (R2) is highlighted by the light-coloured ellipses. d) Sensitivity to the applied tensile stress in the first and second linear regions (R1, R2). Error bars are referred to a pool of 3 independent samples. e) Compressive strain-stress curve of the printed cuboid samples ($15 \times 15 \times 10 \text{ mm}^3$). In the insets, the compression stages of the *HC lattice* structure. f) Resistance response upon pressure loading for *bulk*, *gyroid*, *honeycomb* lattice 3D printed samples.

one. From the mechanical point of view, the high number of voids within the structure results in reduced Young's modulus (Figure S12f). In fact, in the initial stages of compression test, holes collapsed, leading to larger deformations under relatively small loads (Fig. 5e). Once the voids are fully closed, both the *gyroid* and *HC lattice* structures behaves similarly the *bulk* one, as can be seen by the sharp increase in pressure beyond 40 % compressive strain. This is clearly illustrated by the optical images of *HC lattice* sample reported in the insets of Fig. 5e. From the electrical point of view, the great deformability under tiny pressure loads lead to greater variations in electrical resistance at small loads (Fig. 5f).

However, resistance signal for *gyroid* and *HC lattice* sample saturates within a smaller pressure range with respect to *bulk* sample. By computing the sensitivity in the initial pressure linear range between 0 and 1 kPa, it is evident that both *gyroid* and *HC lattice* exhibited enhanced sensitivity to the compressive loads with respect to *bulk* sample. Notably, *HC lattice* geometry displayed a sensitivity 4 times greater than that of the *bulk* sample (Figure S12g).

Additive manufacturing enables precise sensor structuring that fundamentally shapes both electrical and mechanical performance characteristics. This design flexibility allows engineers to create

application-specific architectures: stiffer structures that operate effectively across broader stress ranges with reduced sensitivity, or softer geometries that detect minute loads with enhanced precision. The unprecedented design freedom provided by additive manufacturing, combined with its inherent advantages in material compatibility and fabrication complexity, positions these technologies as transformative tools in advancing soft sensing capabilities.

As practical demonstration once assessed the epidermis compatibility of the material, *METAC-Gly_2* organohydrogel sensors were applied to several parts of a volunteer body to sense mechanical deformations through its piezoresistive transduction method. Large deformations such as the finger bending could be detected by monitoring the resistance pattern of the 3D printed sensors fixed on the forefinger (Fig. 6a). The *re-entrant mesh* displayed the greater resistance variations upon the finger bending, likely due to the improved conformability to the finger surface and therefore an enhanced responsiveness to the mechanical deformations. In addition, if a certain bending angle is kept for some seconds, resistance remained stable (Fig. 6b), demonstrating that, with an appropriate calibration, this sensor could be applied to detect human joint angles. Additionally, smaller deformations were detected as well. In Fig. 6c the sensor, applied to the wrist of the

volunteer, showed the capability of monitor the heartbeat derived by the radial artery pulses. It was also able to monitor the motion of the extrinsic muscles of the fingers, placed on the forearm, as the hand is closed and opened repetitively with different velocities (Fig. 6d). Interestingly, if the volunteer bended consecutively each single finger and thus different muscles are activated, the resistance pattern changed (Fig. 6e). Intensity of resistance signal varied according to the skin deformation in the area where the sensor is placed, becoming higher if the muscular activity is greater. Therefore, information about the bent finger could be gathered indirectly. These examples prove the versatility of the *METAC-Gly_2* organohydrogel flexible sensor in monitoring daily tasks in a low invasive way. However, future challenges need to be considered for effective applications. The multi-stimuli sensing capability enabled by glycerol allows the same material to detect different physical quantities. It is therefore necessary to distinguish which variations in resistance correspond to which specific stimulus. Dummy sensors, hydrophobic encapsulation, or their combination, possibly supported by machine-learning algorithms [104–107], could help decouple different stimuli, facilitating real-world applications. Finally, integration with flexible electronic circuits, flexible power sources, and Bluetooth modules represents the final step toward wireless, real-time

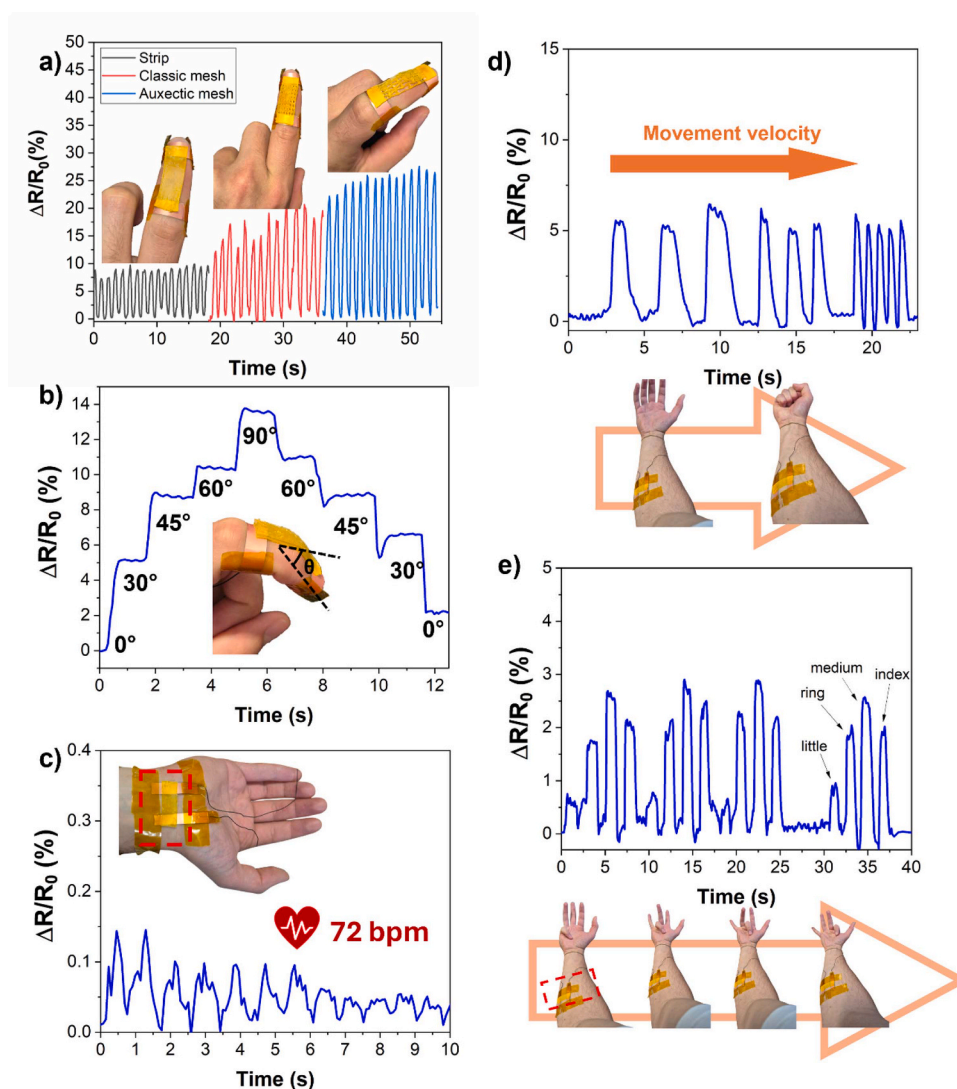


Fig. 6. Applications of *METAC-Gly_2* sensor in human bio-signal detection. (a) Finger bending detected using different 3D printed architectures. (b) Different angles of forefinger bending. (c) Heartbeat acquired at volunteer wrist. (d) Finger muscles detection during several cycles of hand closing and opening at different velocities. In the scheme below, the movement performed, and the sensor position highlighted by red dashed rectangle. (e) Fingers flexor deformation when each finger is bent singularly. In the scheme below, the movements performed, and the sensor position highlighted by red dashed rectangle.

monitoring, enabling applications in healthcare, sports medicine, and wearable devices. This characterization, coupled with its easy manufacturing process, 3D printability, adhesivity, humidity responsiveness, long-term stability and epidermis compatibility, make this material a promising choice for tactile sensors.

3. Conclusion

In summary, a simple one-pot photopolymerization approach was developed to produce a 3D-printable, self-adhesive, transparent, ionically conductive, and epidermis-compatible organohydrogel for flexible wearable sensing applications. The material, obtained by UV polymerization of METAC, a cationic acrylate monomer, crosslinked with PEGDA in a water/glycerol binary solvent, exhibited high stretchability (up to 225 %), a Young's modulus comparable to human tissue, and excellent elastic recovery and energy dissipation under cyclic deformation. The presence of mobile ions within the binary solvent system enabled piezoresistive strain sensing bringing to the development of sensors with highly reproducible and long-term stable mechanical and electrical responses. To evaluate its suitability for epidermal applications, the was, providing a physiologically relevant environment beyond conventional 2D cell cultures. Mostly important, the 3D-printed organohydrogel, interfaced with a mature 3D in vitro epidermis model, confirmed excellent biocompatibility for epidermal applications. Furthermore, DLP-based 3D printing enabled the fabrication of complex architectures, permitting precise modulation of stiffness, mechanical response, and sensitivity tailored to specific applications. The resulting devices successfully monitored diverse human motions, from subtle finger movements to large joint deformations, confirming the versatility and robustness of the ionogel-based sensors. Further works will focus on the integration of the sensors with electronics since the softness of the gel materials represents a very different mechanical compliance of the rigid standard control electronics. Fortunately latest development of flexible electronics should facilitate the integration of both sensors and control boards in a unique system with mechanical compliance adaptable for wearable applications. Overall, the METAC-Gly organohydrogel combines structural tunability, long-term stability, multi-sensing capability, and skin compatibility, establishing it as a promising platform for next-generation wearable electronics, soft robotics, and prosthetic systems.

4. Materials and methods

[2-(Methacryloyloxy)ethyl]trimethylammonium chloride solution (75 wt % in H₂O, METAC), poly (ethylene glycol diacrylate) (average MW 700, PEGDA700), glycerol, lithium phenyl-2,4,6-trimethylbenzoylphosphinate(LAP), tartrazine were purchased from Sigma Aldrich (USA).

Cellular experiments were performed using Human keratinocytes (HaCaT) purchased from Antibody Research Corporation, maintained in Gibco DMEM GlutaMAX high glucose supplemented with 15 % Fetal Bovine Serum (Sigma Aldrich), 1 % penicillin-streptomycin (Sigma Aldrich), 1 % L-glutamine (Sigma Aldrich), 1 % sodium pyruvate (Sigma Aldrich). To perform immunofluorescence, pancytokeratin primary antibody (NovusBio) and filaggrin primary antibody (Invitrogen) were used. 488 anti-mouse secondary antibody (Invitrogen) and 647 anti-rabbit secondary antibody (Invitrogen) were used to obtain the fluorescent signal. For the cytoskeleton, Alexa Fluor™ Plus 555 phalloidin (Invitrogen) was used.

4.1. Tactile sensor preparation

Simple one-pot preparations were employed for ionogel fabrication. For METAC gels, PEGDA700 and TPO-SDS photoinitiator were added in a commercial UV-reactive ionic liquid, the [2-(Methacryloyloxy)ethyl]trimethylammonium chloride (METAC) water solution and mixed for 15

min on a magnetic stirrer (300 rpm, 50°C). Different PEGDA700 weight percentage (0 wt %, 1 wt %, 2 wt %, 5 wt %) with respect to the METAC solution were analysed.

For METAC-Gly_2 gel preparation, 2 wt % of PEGDA 700 and 50 wt % of glycerol with respect to METAC were added to the METAC water solution and stirred for 20 min at 300 rpm at a temperature of 50°C.

LAP photoinitiator weight fraction was fixed at 0.1 wt % with respect to METAC water solution. The photoinitiator was added after solutions cooling at room temperature, by mixing for additional 10 min at 300 rpm.

Flexible sensors samples were prepared by pouring the formulation in polydimethylsiloxane molds. Dumbbell-shaped samples with 30 mm length, 12 mm gauge length, 9 mm width, 3 mm gauge width, and 1.5 mm thickness and a parallelepiped-shaped ones with area 1 cm x 1 cm and thickness of 3 mm were tested. The photopolymerization was performed exposing the samples, placed in a chamber in which nitrogen flux (1 bar) was fluxed, using a Hamamatsu LC8 Lamp (wavelength centered at 365 nm), with an intensity of 35 mW/cm². Oxygen-free atmosphere was necessary to avoid oxygen inhibition at samples upper surface. Samples were exposed 5 min per side.

4.2. Characterization techniques

UV light reactivity of the formulations was assessed through photo-rheologies performed through a rheometer (Physica MCR 302, Anton Paar, Graz, AUT) in the parallel-plate mode (gap 0.2 mm). A 25 mm diameter parallel plate mode with a bottom quartz plate was used to measure the variation of the elastic and viscoelastic moduli after UV irradiation. Photo-rheology tests were performed at a constant strain amplitude of 1 % and a constant shear frequency of 1 Hz to remain in the linear viscoelastic range.

Viscosities of the different formulations were analysed, using an Anton Paar Physica MCR 302 rheometer in 25 mm diameter parallel plate mode. A gap of 0.7 mm between plates was set and rotation shear ramp tests between 0.01 × 1 and 1000 × 1 s⁻¹ were carried out.

For the transmittance evaluation, METAC and METAC-Gly solutions were poured in a 48 well plate (Greiner Bio-One), photopolymerized and the absorbance spectrum from 300nm to 800 nm of the material was measured using Synergy™ HTX Fluorescence Multi-Mode Microplate Reader. The transmittance was calculated as follows:

$$T = e^{-A} * 100 \quad (1)$$

where $A = \frac{(A_{METAC} - A_{PS})}{2 \text{ mm}} * 0.250 \text{ mm}$, since METAC and METAC-Gly sensors (A_{METAC}) were put in a polystyrene well plate (A_{PS}), the thickness of the bottom was 2 mm for the sensors and 0.250 mm for the PS well plate.

A universal testing machine (FZ3-X500, Test Engineering) coupled with a load cell of 500N was employed to evaluate mechanical properties of the cured materials. The measurements were carried out at ambient conditions, as the instrument was not placed in a temperature- and humidity-controlled chamber. Tensile tests were conducted on dumbbell-shaped samples at a velocity of 5 mm min⁻¹ up to rupture. To assess durability over time of samples, they were tested up to a tensile strain of 50 % with the same velocity. Cyclic tensile test was performed stretching dumbbell-shaped samples up to 50 % for 25 subsequent cycles at 10 mm min⁻¹. Copper strips were used as electrodes to acquire the samples electrical resistance.

Hysteresis degree was evaluated as:

$$DH(\%) = 100 \cdot \frac{(E_{load} - E_{unload})}{E_{load}} \quad (2)$$

where E_{load} is the loading energy, namely the area under the loading curve in the σ - ϵ graph and E_{unload} is the area under the unloading curve. In a cycle, the difference between the loading energy and unloading energy is the dissipated energy in that cycle.

Compressive trials were carried out compressing parallelepiped-shaped samples ($10 \times 10 \times 1.5 \text{ mm}^3$) up to 50 N with a velocity of 1 mm min^{-1} . Cyclic compressive tests until 10 N were conducted at the same velocity for 50 cycles. The bottom and the upper aluminium plates of the compressive setup were used as electrodes.

Adhesion tests were carried out using a 180° peel configuration. Samples with nominal dimensions of $15 \times 15 \times 1.5 \text{ mm}^3$ were sandwiched between two surfaces of the material under investigation. A weight of 50 g was applied to the assembled samples and kept for 3 min. Glass, copper, wood, pigskin and cotton were considered. Copper, pigskin and cotton substrates were glued on a rigid glass supports. A constant tensile velocity was set at 5 mm min^{-1} . Adhesive strength was computed dividing the maximum force applied with the effective contact area.

Tensile and compressive mechanical trials were coupled with the electrical measurement of the sample impedance, through a LCR meter (BK 894, B&K Precision). Impedance was measured applying an AC voltage of 0.5 V at 1 kHz and was modelled by a parallel between a resistor (R_p) and a capacitor (C_p).

Conductivity was evaluated via electrochemical impedance spectroscopy (EIS) measurements, which were carried out applying a small AC voltage signal (10 mV) within a frequency range 1 MHz–10 MHz. High frequency resistance (R_{hf}), was used to calculate the ionic conductivity of the hydrogels/organohydrogels. For this purpose, the eutectogels were placed between two parallel stainless-steel plates, and the conductivity (σ) was calculated according to the equation:

$$\sigma = \frac{d}{R_{hf} \cdot A} \quad (3)$$

where d is the distance between the two electrodes and A is the gel's area.

Samples responsiveness to humidity was assessed by using a climatic chamber (KeyKratos™ Plus 01.05.XX). Temperature was fixed at 25°C and relative humidity (RH) was increased from 40 % to 95 % with intermediate steps at 50 %, 60 %, 70 %, 80 %, 85 %, 90 %, 92.5 %. Resistance and capacitance of sensors were acquired for each RH step through 1-minute-long acquisition once the chamber humidity was stable. The average values over the acquisition time were then considered.

Relative resistance variations are computed as follows:

$$\frac{\Delta R}{R_0} (\%) = \frac{R - R_0}{R_0} \cdot 100 \quad (4)$$

where R is the resistance at a certain external stimulus applied and R_0 is the resistance of the sample when no external stimuli are applied.

Sensitivity (S) for piezoresistive transduction mode to the external stimuli was evaluated using the following formula:

$$S = \frac{\frac{\Delta R}{R_0}}{X} \quad (5)$$

where $\frac{\Delta R}{R_0}$ is the relative resistance variation and, X is the value of the external stimulus applied (tensile strain, compressive strain or humidity).

4.3. 3D printing

The glycerol-based UV reactive formulation was processed using a commercial DLP printer (Asiga MAX X UV385) operating at a nominal resolution of $27 \times 27 \mu\text{m}$ [2] and 385 nm wavelength. First, tartrazine was added at 0.05 wt % with respect of METAC, as dye to improve resolution. The dye was dispersed by stirring at 300 rpm for 5 min at room temperature. The layer thickness was defined as 25 μm , with a separation velocity set at 0.5 mm s^{-1} and an approach velocity of 1 mm s^{-1} . A wait of 1.2 seconds was applied before irradiation. For enhancing

adhesion of the architectures on the printing head, 12 burn-in layers were set and irradiated at 5 mW cm^{-2} for 6.2 seconds. The subsequent layers were irradiated at 4 mW cm^{-2} for 5.2 seconds. Samples were cleaned through compressed air to remove unreacted resin and then with a cloth soaked in ethanol. Post-curing was carried out through a UV oven (Robofactory UV) for 4 min. To facilitate samples handling reducing their adhesiveness, they were coated by talc powder. Before electromechanical testing, the talc powder was wiped off with a cloth soaked in distilled water.

The 3D printed architectures tested under tensile loading (strip, classic and re-entrant mesh) had dimension of $30 \times 10 \times 2 \text{ mm}^3$. The 3D structures examined under compression (bulk, gyroid, honeycomb lattice) measured $15 \times 15 \times 10 \text{ mm}^3$.

4.4. Cytotoxicity evaluation

To test the cytotoxicity, samples of METAC_2 gel (1 cm of diameter and 4 mm of thickness) were photopolymerized and then sterilized with germicide ultraviolet light (30 min each side). Samples (2 samples in 10 mm) were then incubated with complete DMEM for 72 h. This conditioned medium was then collected and used for cell culture.

1×10^4 HaCaT, were seeded onto a 96 well plate (TC treated, Greiner Bio-One) and cultured with the conditioned medium for 72 h at 37°C at 5 % CO_2 . After 24 h and 72 h MTT assay at the concentration of 0.5 mg/ml was used to evaluate the viability at each time point. After 2 h of incubation at 37°C , the formazan salts were dissolved in 200 μl of DMSO and the absorbance at 570 nm (650 nm reference wavelength) was evaluated using Synergy™ HTX Fluorescence Multi-Mode Microplate Reader. The signal of the normal and conditioned medium without cells was used as background. The cell proliferation experiments were performed three times. Differences between groups were analysed by two-way ANOVA

4.5. 3D in vitro epidermis model

The 3D *in vitro* epidermis model was obtained in a similar way to the epidermal compartment of a previously biofabricated 3D *in vitro* skin model [55]. Briefly, HaCaT cells were seeded on top of PET 12-well hanging inserts, with a porosity of $0.4 \mu\text{m}$ (Millicell®), using 2×10^5 cells/insert. The first 3 days of culture were performed as submerged culture, in complete DMEM. Specifically, this involved using 1.5 ml of medium in the lower compartment and 1 ml in the upper compartment. This phase was necessary to facilitate the adhesion of keratinocytes to the insert membrane. After the first 3 days, Air Liquid Interface (ALI) culture started, supplying 500 μl of 3dGRO™ Skin Differentiation Medium (Sigma) in the lower compartment and leaving the upper compartment in contact with air. Culture proceeds for a total of 5 weeks and the medium was changed every 2 days. After the epidermis maturation, sensors of 6 mm of diameter and 1.5 mm of thickness were placed on top of the epidermis model. The sensors were gently placed on top of the epidermal surface without applying external pressure, in order to mimic passive skin–sensor contact. The models were maintained at the air–liquid interface, under static condition, with culture medium supplied exclusively from the basal side, ensuring physiological epidermal exposure conditions. Tests were made both with METAC and METAC-Gly_2 gels. The models were analysed after 1h, 6h and 24h to evaluate potential epidermal damage.

4.6. Immunofluorescence

3D *in vitro* epidermal models were stained after 1h, 6h and 24h after the sensor positioning. Specifically, the samples were fixed in paraformaldehyde 4 v/v % in DPBS (J61899.AK, Thermo Scientific) for 1 h at RT. For staining, fixed samples were washed in DPBS, permeabilized with 0.25 v/v % of Triton X-100 (Sigma-Aldrich) for 15 min and blocked with a solution of 5 w/v% BSA (Sigma-Aldrich) and 0.1 v/v% Tween

(Sigma-Aldrich) for 1 h. For the epidermal model analysis, two different antibodies were used at specific dilution: pancyokeratin (2 µg/ml, NovusBio) and filaggrin (10 µg/ml, Invitrogen). Specifically, primary antibodies were incubated overnight at 4°C and after three washing steps in DPBS supplemented with 0.1v/v% Tween, the staining with appropriate secondary antibodies lasted 1h at RT. Nuclei were stained with a solution of 1 µM DAPI and 11 µM Alexa Fluor™ Plus 555 phalloidin (Invitrogen) in PBS for 30 min. At the end, samples were analyzed using a microscope (Eclipse Ti2 Nikon, Tokyo, Japan) equipped with a Crest X-Light spinning disk confocal microscope.

4.7. Live and dead evaluation

LIVE/DEAD cell assay kit (Sigma Aldrich) was used to evaluate cell viability after 1, 6, 24 and 48 hours following sensor positioning. In detail, the 3D in vitro epidermal models were washed twice with DPBS, stained with 1.5 µM Propidium Iodide (PI) and 1µM Calcein-AM for 30 min in an incubator at 37°C and washed again with DPBS to remove the unreacted dyes. The fluorescence signals were detected using an Eclipse Ti2 Nikon (Tokyo, Japan) microscope equipped with a Crest X-Light spinning disk. For the quantification of cell viability, fluorescence images were processed using the Fiji/ImageJ software. Due to high cellular confluence hindering individual cell counting, a pixel-based area coverage analysis was performed. Briefly, the composite images were split into their respective green (live) and red (dead) channels. A global threshold was applied to each channel to generate binary masks representing the total area occupied by live and dead populations. The percentage of the field of view occupied by each signal was calculated using the Area Fraction parameter within the Set Measurements menu, ensuring the Limit to Threshold option was enabled. Cell viability was then expressed as the ratio of the area occupied by live cells (A_{live}) to the total area occupied by both live and dead cells ($A_{live} + A_{dead}$) according to the formula:

$$Viability (\%) = 100 \cdot A_{live} / (A_{live} + A_{dead}) \quad (6)$$

CRediT authorship contribution statement

Giorgio Mogli: Writing – original draft, Methodology, Investigation, Formal analysis, Data curation, Conceptualization. **Simona Villata:** Writing – original draft, Investigation, Formal analysis, Conceptualization. **Annalisa Chiappone:** Writing – review & editing, Validation, Resources, Funding acquisition, Conceptualization. **Francesca Frascella:** Writing – review & editing, Validation, Methodology, Funding acquisition, Conceptualization. **Stefano Stassi:** Writing – review & editing, Writing – original draft, Validation, Supervision, Resources, Methodology, Conceptualization.

Declaration of competing interest

The authors declare that they have no known competing financial interests or personal relationships that could have appeared to influence the work reported in this paper.

Acknowledgements

This research was supported by the Ministero dell'Università e della Ricerca (MUR), through PRIN 2022 - PASSO Prot.2022TKNRJ grant and the National Plan for Complementary Investments to the NRRP, project "D3-4Health - Digital Driven Diagnostics, prognostics and therapeutics for sustainable Health care" (project code:PNC0000001).

Supplementary materials

Supplementary material associated with this article can be found, in the online version, at [doi:10.1016/j.apmt.2026.103148](https://doi.org/10.1016/j.apmt.2026.103148).

Data availability

Data will be made available on request.

References

- [1] S. Chen, S. Fan, H. Chan, Z. Qiao, J. Qi, Z. Wu, J.C. Yeo, C.T. Lim, Liquid metal functionalization innovations in wearables and soft robotics for smart healthcare applications, *Adv. Funct. Mater.* 34 (31) (2023) 2309989.
- [2] L. Liu, Z. Ai, X. Zhang, K. Tang, Y. Pei, Flexible and robust polyaniline/cross-linked collagen sponge with fibrils network structure as a piezoresistive sensing material, *Int. J. Biol. Macromol.* 279 (Pt 3) (2024) 135305.
- [3] C. Peng, Y. Chen, B. Yang, Z. Jiang, Y. Liu, Z. Liu, L. Zhou, L. Tang, Recent advances of soft actuators in smart wearable electronic-textile, *Adv. Mater. Technol.* 9 (15) (2024) 2400079.
- [4] G. Mogli, M. Costantini, S. Stassi, Highly sensitive PDMS-Ag nanoflakes porous pressure sensors prepared by templating and molding approaches for wearable applications, *Sens. Actuators A: Phys.* 392 (2025) 116734.
- [5] A. Shen, H. Xuan, Y. Jia, S. Gu, R.E. Neisiany, W. Shu, W. Sun, Z. You, Dynamic healing-assembly for biocompatible, biodegradable, stretchable and self-healing triboelectric nanogenerators, *Chem. Eng. J.* 491 (2024) 151896.
- [6] W. Wang, Y. Jiang, D. Zhong, Z. Zhang, S. Choudhury, J.C. Lai, H. Gong, S. Niu, X. Yan, Y. Zheng, C.C. Shih, R. Ning, Q. Lin, D. Li, Y.H. Kim, J. Kim, Y.X. Wang, C. Zhao, C. Xu, X. Ji, Y. Nishio, H. Lyu, J.B. Tok, Z. Bao, Neuromorphic sensorimotor loop embodied by monolithically integrated, low-voltage, soft e-skin, *Science* 380 (6646) (2023) 735–742.
- [7] X. Xun, Z. Zhang, X. Zhao, B. Zhao, F. Gao, Z. Kang, Q. Liao, Y. Zhang, Highly robust and self-powered electronic skin based on tough conductive self-healing elastomer, *ACS Nano* 14 (7) (2020) 9066–9072.
- [8] S. Zhang, S. Li, Z. Xia, K. Cai, A review of electronic skin: soft electronics and sensors for human health, *J. Mater. Chem. B* 8 (5) (2020) 852–862.
- [9] H.R. Lim, H.S. Kim, R. Qazi, Y.T. Kwon, J.W. Jeong, W.H. Yeo, Advanced soft materials, sensor integrations, and applications of wearable flexible hybrid electronics in healthcare, energy, and environment, *Adv. Mater.* 32 (15) (2020) e1901924.
- [10] S. Stassi, V. Cauda, G. Canavese, C.F. Pirri, Flexible tactile sensing based on piezoresistive composites: a review, *Sens. (Basel)* 14 (3) (2014) 5296–5332.
- [11] X. Gao, J. Su, C. Xu, S. Cao, S. Gu, W. Sun, Z. You, Water-based continuous fabrication of highly elastic electromagnetic fibers, *ACS Nano* 18 (27) (2024) 17913–17923.
- [12] Y. Gu, Y. Luo, Q. Guo, W. Yu, P. Li, X. Wang, T. Ye, H. Chang, W. Yuan, H. Wu, J. Wu, K. Tao, Empowering human-machine interfaces: self-powered hydrogel sensors for flexible and intelligent systems, *Adv. Funct. Mater.* 36 (5) (2025) e09085.
- [13] H. Yuk, B. Lu, X. Zhao, Hydrogel bioelectronics, *Chem. Soc. Rev.* 48 (6) (2019) 1642–1667.
- [14] M. Han, D. Luo, K. Talha, J. He, M. Xing, L. Chen, H. Liu, Research progress on conductive hydrogels and their applications in flexible sensors: a review, *J. Mater. Chem. A* 13 (24) (2025) 18062–18080.
- [15] C. Ji, Y. Wang, Q. Qi, Y. Li, L. Cao, Electrically conductive hydrogels for flexible wearable devices: materials, design, and applications, *Adv. Mater. Technol.* 10 (21) (2025) e01044.
- [16] J. Yan, L. Wang, C. Zhao, D. Xiang, H. Li, J. Lai, B. Wang, Z. Li, H. Lu, H. Zhou, Y. Wu, Stretchable semi-interpenetrating carboxymethyl guar gum-based composite hydrogel for moisture-proof wearable strain sensor, *Langmuir* 39 (3) (2023) 1061–1071.
- [17] X. Ma, X. Shi, Y. Wang, W. Xiong, C. Xiong, J. Yang, L. You, S. Wang, Stretchable porous conductive hydrogel films prepared by emulsion template method as flexible sensors, *Colloids Surf. A: Physicochem. Eng. Asp.* 676 (2023) 132272.
- [18] H. Wang, S.K. Biswas, S. Zhu, Y. Lu, Y. Yue, J. Han, X. Xu, Q. Wu, H. Xiao, Self-healable electro-conductive hydrogels based on core-shell structured nanocellulose/carbon nanotubes hybrids for use as flexible supercapacitors, *Nanomaterials* 10 (1) (2020) 112.
- [19] F. Lin, Y. Qiu, X. Zheng, Z. Duanmu, Q. Lu, B. Huang, L. Tang, B. Lu, One-pot mechanochemical assembly of lignocellulose nanofiber/graphite nanocomposites for wearable electronic devices, *Chem. Eng. J.* 437 (2022) 135286.
- [20] Y. Li, X. Liu, L. Han, Z. Lu, L. Liu, High mass loading of polypyrrole in conductive hydrogels for stretchable all-in-one supercapacitors and self-powered strain sensing system, *J. Electroanal. Chem.* 950 (2023) 117904.
- [21] Y.Z.N. Htwe, S. Pawłowska, M. Jaafar, Emerging strategies for the fabrication of conductive hydrogels from conductive polymers and their composites for wearable sensors, energy storage, and biosensor applications: methods, mechanisms, and future perspectives, *Adv. Mater. Technol.* (2025) e01845 n/an/a.
- [22] G. Mogli, A. Chiappone, A. Sacco, C.F. Pirri, S. Stassi, Ultrasensitive piezoresistive and piezocapacitive cellulose-based ionic hydrogels for wearable multifunctional sensing, *ACS Appl. Electron. Mater.* 5 (1) (2022) 205–215.
- [23] L. Zeng, B. Liu, L. Duan, G. Gao, Tough, recyclable and biocompatible carrageenan-modified polyvinyl alcohol ionic hydrogel with physical cross-linked for multimodal sensing, *Int. J. Biol. Macromol.* 253 (Pt 4) (2023) 126954.
- [24] D. Won, J. Bang, S.H. Choi, K.R. Pyun, S. Jeong, Y. Lee, S.H. Ko, Transparent electronics for wearable electronics application, *Chem. Rev.* 123 (16) (2023) 9982–10078.

- [25] S. Yan, Y. Chen, D. Li, Y. Zheng, X. Fu, B. Yu, S. Chen, C. Ni, H. Qi, W. Zhou, Mechanically robust, transparent, conductive hydrogels based on hydrogen bonding, ionic coordination interactions and electrostatic interactions for light-curing 3D printing, *Chem. Eng. J.* 486 (2024) 150289.
- [26] F. Fu, J. Wang, H. Zeng, J. Yu, Functional conductive hydrogels for bioelectronics, *ACS Mater. Lett.* 2 (10) (2020) 1287–1301.
- [27] M. Sher, L.A. Shah, L. Ara, R. Ullah, M. Khan, H.-M. Yoo, J. Fu, Xanthan gum toughen ionically conductive hydrogels for flexible and artificial epidermis sensors with multifunctionality and self-healability, *Sens. Actuators A: Phys.* 370 (2024) 115199.
- [28] G. Mogli, M. Reina, A. Chiappone, A. Lamberti, C.F. Pirri, I. Roppolo, S. Stassi, Self-powered integrated tactile sensing system based on ultrastretchable, self-healing and 3D printable ionic conductive hydrogel, *Adv. Funct. Mater.* 34 (7) (2024) 2307133.
- [29] J. Cui, R. Xu, W. Dong, T. Kaneko, M. Chen, D. Shi, Skin-inspired patterned hydrogel with strain-stiffening capability for strain sensors, *ACS Appl. Mater. Interfaces* 15 (41) (2023) 48736–48743.
- [30] G.C. Luque, M.L. Picchio, A.P.S. Martins, A. Dominguez-Alfaro, N. Ramos, I. del Agua, B. Marchiori, D. Mecerreyes, R.J. Minari, L.C. Tomé, 3D printable and biocompatible ionogels for body sensor applications, *Adv. Electron. Mater.* 7 (8) (2021) 2100178.
- [31] W. Li, F. Wang, J. Liu, J. Wang, L. Deng, Super-adhesive and highly sensitive conductive hydrogel based on halometallate ionic liquid for flexible electronic devices, *Chem. Eng. J.* 519 (2025) 165699.
- [32] K. Lei, M. Chen, P. Guo, J. Fang, J. Zhang, X. Liu, W. Wang, Y. Li, Z. Hu, Y. Ma, H. Jiang, J. Cui, J. Li, Environmentally adaptive polymer hydrogels: maintaining wet-soft features in extreme conditions, *Adv. Funct. Mater.* 33 (41) (2023) 2303511.
- [33] C. Xu, K. Yang, G. Zhu, C. Ou, J. Jiang, E. Zhuravlev, Y. Zhang, Anti-freezing multifunctional conductive hydrogels: from structure design to flexible electronic devices, *Mater. Chem. Front.* 8 (2) (2024) 381–403.
- [34] A.S.D. Ferreira, R. Craveiro, A.R. Duarte, S. Barreiros, E.J. Cabrita, A. Paiva, Effect of water on the structure and dynamics of choline chloride/glycerol eutectic systems, *J. Mol. Liq.* 342 (2021) 117463.
- [35] M.A. Kuzina, D.D. Kartsev, A.V. Stratonovich, P.A. Levkin, Organogels versus hydrogels: advantages, challenges, and applications, *Adv. Funct. Mater.* 33 (27) (2023) 2301421.
- [36] S. Xiang, X. He, F. Zheng, Q. Lu, Multifunctional flexible sensors based on ionogel composed entirely of ionic liquid with long alkyl chains for enhancing mechanical properties, *Chem. Eng. J.* 439 (2022) 135644.
- [37] S. Al-Sodies, A.M. Asiri, A. Khan, K.A. Alamry, M.A. Hussein, Recent exploiting of poly(ionic liquid)s in sensing applications, *Eur. Polym. J.* 205 (2024) 112719.
- [38] Z. Wang, J. Zhang, J. Liu, S. Hao, H. Song, J. Zhang, 3D printable, highly stretchable, superior stable ionogels based on poly(ionic liquid) with hyperbranched polymers as macro-cross-linkers for high-performance strain sensors, *ACS Appl. Mater. Interfaces* 13 (4) (2021) 5614–5624.
- [39] J. Sun, S. Zhou, Z. Zhao, F. Zhang, Z. Guo, S. Liu, Y. Lu, Facile fabrication of a stretchable, stable, and self-adhesive poly(ionic liquid) as a flexible sensor, *RSC Appl. Polym.* 2 (2) (2024) 205–213.
- [40] Z. Guo, H. Zhang, W. Xie, A. Tang, W. Liu, 3D printing hydrogel with structural design via vat photopolymerization for strain sensing, *Addit. Manuf.* 77 (2023) 103824.
- [41] G. Mogli, I. Roppolo, A. Chiappone, S. Stassi, Multi-responsive 3D printable organohydrogel for the fabrication of durable and low-hysteresis flexible sensors, *Appl. Mater. Today* 44 (2025) 102675.
- [42] R. Si, Y. Wang, Y. Yang, Y. Wu, M. Wang, B. Han, A multifunctional conductive organohydrogel as a flexible sensor for synchronous real-time monitoring of traumatic wounds and pro-healing process, *Chem. Eng. J.* 489 (2024) 151419.
- [43] S. Jiang, Y. Wang, M. Tian, H. Zhang, R. Wang, H. Yan, H. Tan, R. Esmacely Neisiany, W. Sun, Z. You, Readily recyclable, degradable, stretchable, highly conductive, anti-freezing and anti-drying glycerohydrogel for triboelectric nanogenerator, *Chem. Eng. J.* 504 (2025) 158881.
- [44] G.C. Luque, M.L. Picchio, A.P.S. Martins, A. Dominguez-Alfaro, L.C. Tome, D. Mecerreyes, R.J. Minari, Elastic and thermoreversible ionogels by supramolecular PVA/phenol interactions, *Macromol. Biosci.* 20 (11) (2020) e2000119.
- [45] H. Huang, L. Sun, Y. Zhang, R. Zhang, C. Chen, W. Sun, Ionogels reinforced by ionophoric coordination, *Adv. Mater.* 37 (34) (2025) e2506563.
- [46] T. Lu, S. Ji, W. Jin, Q. Yang, Q. Luo, T.L. Ren, Biocompatible and long-term monitoring strategies of wearable, ingestible and implantable biosensors: reform the next generation healthcare, *Sens. (Basel)* 23 (6) (2023) 2991.
- [47] S. Najafikhoshnoo, T. Kim, J.A. Tavares-Negrete, X. Pei, P. Das, S.W. Lee, J. Rajendran, R. Esfandyarpour, A 3D nanomaterials-printed wearable, battery-free, biocompatible, flexible, and wireless pH sensor system for real-time health monitoring, *Adv. Mater. Technol.* 8 (8) (2023) 2201655.
- [48] P. Bhushan, Y. Umasankar, J.D. Hutcheson, S. Bhansali, Toxicity assessment of wearable wound sensor constituents on keratinocytes, *Toxicol. Vitro.* 58 (2019) 170–177.
- [49] M. Kapalczyńska, T. Kolenda, W. Przybyła, M. Zajackowska, A. Teresiak, V. Filas, M. Ibbes, R. Blizniak, L. Luczewski, K. Lamperska, 2D and 3D cell cultures - a comparison of different types of cancer cell cultures, *Arch. Med. Sci.* 14 (4) (2018) 910–919.
- [50] K. Duval, H. Grover, L.H. Han, Y. Mou, A.F. Pegoraro, J. Fredberg, Z. Chen, Modeling physiological events in 2D vs. 3D cell culture, *Physiol. (Bethesda)* 32 (4) (2017) 266–277.
- [51] B.S. Kim, G. Gao, J.Y. Kim, D.W. Cho, 3D cell printing of perfusable vascularized human skin equivalent composed of epidermis, dermis, and hypodermis for better structural recapitulation of native skin, *Adv. Heal. Mater.* 8 (7) (2019) e1801019.
- [52] J. Kober, A. Gugerell, M. Schmid, L.P. Kamolz, M. Keck, Generation of a fibrin based three-layered skin substitute, *Biomed. Res. Int.* 2015 (2015) 170427.
- [53] A. Baroni, E. Buommino, V. De Gregorio, E. Ruocco, V. Ruocco, R. Wolf, Structure and function of the epidermis related to barrier properties, *Clin. Dermatol.* 30 (3) (2012) 257–262.
- [54] E. Sutterby, P. Thurgood, S. Baratchi, K. Khoshmanesh, E. Pirogova, Microfluidic skin-on-a-chip models: toward biomimetic artificial skin, *Small* 16 (39) (2020) e2002515.
- [55] S. Villata, D. Baruffaldi, R. Cue Lopez, C. Paoletti, P. Bosch, L. Napione, A. M. Giovannozzi, C.F. Pirri, E. Martinez-Campos, F. Frascella, Broadly accessible 3D in vitro skin model as a comprehensive platform for antibacterial therapy screening, *ACS Appl. Mater. Interfaces* 16 (51) (2024) 70284–70296.
- [56] C. Ma, J. Wei, Y. Zhang, X. Chen, C. Liu, S. Diao, Y. Gao, K. Matyjaszewski, H. Liu, Highly processable ionogels with mechanical robustness, *Adv. Funct. Mater.* 33 (31) (2023) 2211771.
- [57] J. Zhu, H. Gao, Z. Zheng, Y. Cao, T. Wang, R. Kumar Kankala, L. Wu, A.-Z. Chen, S.-B. Wang, Y. Li, Photocuring 3D printable flexible strain sensor enhanced by in situ grown silk fibroin nanoparticles, *Chem. Eng. J.* 497 (2024) 154762.
- [58] C. Zhang, H. Zheng, J. Sun, Y. Zhou, W. Xu, Y. Dai, J. Mo, Z. Wang, 3D printed, solid-state conductive ionoelastomer as a generic building block for tactile applications, *Adv. Mater.* 34 (2) (2022) e2105996.
- [59] I. Kurokawa, H. Mizutani, K. Kusumoto, S. Nishijima, M. Tsujita-Kyutoku, N. Shikata, A. Tsubura, Cytokeratin, filaggrin, and p63 expression in reepithelialization during human cutaneous wound healing, *Wound Repair Regen.* 14 (1) (2006) 38–45.
- [60] T. Shiga, H. Mori, K. Uemura, R. Moriuchi, H. Dohra, A. Yamawaki-Ogata, Y. Narita, A. Saito, Y. Kotsuchibashi, Evaluation of the bactericidal and fungicidal activities of poly([2-(methacryloyloxy)ethyl]trimethyl ammonium chloride)(poly(METAC))-based materials, *Polym. (Basel)* 10 (9) (2018) 947.
- [61] L. Jiang, J. Liu, S. He, A. Liu, J. Zhang, H. Xu, W. Shao, Flexible wearable sensors based on lignin doped organohydrogel with multi-functionalities, *Chem. Eng. J.* 430 (2022) 132653.
- [62] K. Bakshi, S. Mitra, V.K. Sharma, M.S.K. Jayadev, V.G. Sakai, R. Mukhopadhyay, A. Gupta, S.K. Ghosh, Imidazolium-based ionic liquids cause mammalian cell death due to modulated structures and dynamics of cellular membrane, *Biochim. Biophys. Acta Biomembr.* 1862 (2) (2020) 183103.
- [63] A. Romero, A. Santos, J. Tojo, A. Rodriguez, Toxicity and biodegradability of imidazolium ionic liquids, *J. Hazard Mater.* 151 (1) (2008) 268–273.
- [64] M.A. Smirnov, V.S. Fedotova, M.P. Sokolova, A.L. Nikolaeva, V.Y. Elokhoysky, M. Karttunen, Polymerizable choline- and imidazolium-based ionic liquids reinforced with bacterial cellulose for 3D-printing, *Polym. (Basel)* 13 (18) (2021) 3044.
- [65] X. He, J. Dong, X. Zhang, X. Bai, C. Zhang, D. Wei, Self-Healing, Anti-Fatigue, antimicrobial ionic conductive hydrogels based on Choline-Amino acid polyionic liquids for Multi-Functional sensors, *Chem. Eng. J.* 435 (Pt 2) (2022) 135168.
- [66] G. Melilli, I. Carmagnola, C. Tonda-Turo, F. Pirri, G. Ciardelli, M. Sangermano, M. Hakkarainen, A. Chiappone, DLP 3D printing meets lignocellulosic biopolymers: carboxymethyl cellulose inks for 3D biocompatible hydrogels, *Polym. (Basel)* 12 (8) (2020) 1655.
- [67] M. Kang, H.-G. Choi, K. Park, S. Pyo, Additively manufactured 3D auxetic metamaterials for structurally guided capacitive and resistive tactile sensing, *Adv. Funct. Mater.* 35 (47) (2025) e2510.
- [68] K. Wu, S. Peng, A. Hedoux, E. Shalaev, Water structure in glycerol: Spectroscopic and computer simulation investigation of hydrogen bonding and water clustering, *J. Mol. Liq.* 355 (2022) 118916.
- [69] F. Gabriele, M. Chiarini, R. Germani, M. Tiecco, N. Spreti, Effect of water addition on choline chloride/glycol deep eutectic solvents: Characterization of their structural and physicochemical properties, *J. Mol. Liq.* 291 (2019) 111301.
- [70] T. Kuhn, F.L.C. Morgan, M.B. Baker, L. Moroni, An efficient and easily adjustable heating stage for digital light processing set-ups, *Addit. Manuf.* 46 (2021) 102102.
- [71] L. Strohmeyer, H. Frommwald, S. Schlogl, Digital light processing 3D printing of modified liquid isoprene rubber using thiol-click chemistry, *RSC Adv.* 10 (40) (2020) 23607–23614.
- [72] Kuzina, M. A.; Kartsev, D. D.; Stratonovich, A. V.; Levkin, P. A., Organogels versus hydrogels: advantages, challenges, and applications. 2023, 33 (27), 2301421.
- [73] Z. He, W. Yuan, Adhesive, stretchable, and transparent organohydrogels for antifreezing, antidyrring, and sensitive ionic skins, *ACS Appl. Mater. Interfaces* 13 (1) (2021) 1474–1485.
- [74] S. Cui, S. Zhang, F. Zhang, R. Lin, C. Tang, X. Jing, Tannic acid-coated cellulose nanocrystal-reinforced transparent multifunctional hydrogels with UV-filtering for wearable flexible sensors, *Carbohydr. Polym.* 323 (2024) 121385.
- [75] T. Zhu, Y. Ni, G.M. Biesold, Y. Cheng, M. Ge, H. Li, J. Huang, Z. Lin, Y. Lai, Recent advances in conductive hydrogels: classifications, properties, and applications, *Chem. Soc. Rev.* 52 (2) (2023) 473–509.
- [76] K. Kim, Y.G. Park, B.G. Hyun, M. Choi, J.U. Park, Recent advances in transparent electronics with stretchable forms, *Adv. Mater.* 31 (20) (2019) e1804690.
- [77] D. Arunbabu, H. Shahsavani, W. Zhang, B. Zhao, Poly(AAc-co-MBA) hydrogel films: adhesive and mechanical properties in aqueous medium, *J. Phys. Chem. B* 117 (1) (2013) 441–449.
- [78] L. Zhu, Y. Pan, J. Wu, Z. Du, Z.-B. Shao, Polyelectrolyte microgels-enhanced double-crosslinking polyacrylamide hydrogel sensing with stretchable, transparent, and fast response, *Eur. Polym. J.* 200 (2023) 112517.

- [79] S. Zeng, J. Zhang, G. Zu, J. Huang, Transparent, flexible, and multifunctional starch-based double-network hydrogels as high-performance wearable electronics, *Carbohydr. Polym.* 267 (2021) 118198.
- [80] Y. Li, N. Li, W. Liu, A. Prominski, S. Kang, Y. Dai, Y. Liu, H. Hu, S. Wai, S. Dai, Z. Cheng, Q. Su, P. Cheng, C. Wei, L. Jin, J.A. Hubbell, B. Tian, S. Wang, Achieving tissue-level softness on stretchable electronics through a generalizable soft interlayer design, *Nat. Commun.* 14 (1) (2023) 4488.
- [81] B. Yang, W. Yuan, Highly stretchable and transparent double-network hydrogel ionic conductors as flexible thermal-mechanical dual sensors and electroluminescent devices, *ACS Appl. Mater. Interfaces* 11 (18) (2019) 16765–16775.
- [82] L. Xu, X. Li, J. Gao, M. Yan, Q. Wang, Environment-tolerant gelatin based ionic conductive organohydrogel for flexible sensor, *Mater. Today Commun.* 40 (2024) 109542.
- [83] Q. Yu, Z. Qin, F. Ji, S. Chen, S. Luo, M. Yao, X. Wu, W. Liu, X. Sun, H. Zhang, Y. Zhao, F. Yao, J. Li, Low-temperature tolerant strain sensors based on triple crosslinked organohydrogels with ultrastretchability, *Chem. Eng. J.* 404 (2021) 126559.
- [84] A. Zhagiparova, G. Kalimuldina, A.L. Diaby, F. Abbassi, M.H. Ali, S. Araby, Key factors and performance criteria of wearable strain sensors based on polymer nanocomposites, *Nano Futures* 7 (2) (2023) 022001.
- [85] Y. Wang, Y. Jia, H. Ren, C. Lao, W. Peng, B. Feng, J. Wang, A mechanical, electrical dual autonomous self-healing multifunctional composite hydrogel, *Mater. Today Bio.* 12 (2021) 100138.
- [86] J.J. Paik, B. Jang, S. Nam, L.J. Guo, A transparent poly(vinyl alcohol) ion-conducting organohydrogel for skin-based strain-sensing applications, *Adv. Heal. Mater.* 12 (22) (2023) e2300076.
- [87] Y. Liu, G. Tian, Y. Du, P. Shi, N. Li, Y. Li, Z. Qin, T. Jiao, X. He, Highly stretchable, low-hysteresis, and adhesive TA@MXene-composited organohydrogels for durable wearable sensors, *Adv. Funct. Mater.* 34 (30) (2024) 2315813.
- [88] Z. Li, J. Wang, R. Hu, C. Lv, J. Zheng, A highly ionic conductive, healable, and adhesive polysiloxane-supported ionogel, *Macromol. Rapid Commun.* 40 (7) (2019) e1800776.
- [89] X. Li, N. Luo, Z. Li, P. Li, J. Chang, L. Fang, Q. Huang, B. Zhu, Y. Zhang, X. Zhou, Z. Zheng, Z. Xie, Polymerizable deep eutectic solvents-enabled high-lignin-density networks for ambient multi-scale fabrication of multifunctional and extreme environment adaptable soft devices, *Adv. Mater.* (2026) e19633 n/an/a.
- [90] Y. Oz, A. Roy, S. Jain, Y. Zheng, E. Mahmood, A. Baidya, N. Annabi, Designing a naturally inspired conductive copolymer to engineer wearable bioadhesives for sensing applications, *ACS Appl. Mater. Interfaces* 16 (28) (2024) 36002–36016.
- [91] Y. Ohm, C. Pan, M.J. Ford, X. Huang, J. Liao, C. Majidi, An electrically conductive silver–polyacrylamide–alginate hydrogel composite for soft electronics, *Nat. Electron.* 4 (3) (2021) 185–192.
- [92] J. Liu, H. Zheng, P.S. Poh, H.G. Machens, A.F. Schilling, Hydrogels for engineering of perfusable vascular networks, *Int. J. Mol. Sci.* 16 (7) (2015) 15997–16016.
- [93] J.T. Ault, S. Shin, A. Garcia, A. Perazzo, H.A. Stone, Viscosity measurements of glycerol in a parallel-plate rheometer exposed to atmosphere, *J. Fluid Mech.* 968 (2023) A2.
- [94] X. Dang, B. Guo, Y. Fu, Y. Fei, X. Wang, All-natural biomass-based multifunctional conductive hydrogel for an all-in-one wearable strain sensor, *Cell Biomater.* 1 (5) (2025) 100076.
- [95] G. Bovone, O.Y. Dudaryeva, B. Marco-Dufort, M.W. Tibbitt, Engineering hydrogel adhesion for biomedical applications via chemical design of the junction, *ACS Biomater. Sci. Eng.* 7 (9) (2021) 4048–4076.
- [96] H. Zhong, W. Shan, L. Liang, X. Jiang, L. Wu, High stretchable and self-adhesive multifunctional hydrogel for wearable and flexible sensors, *Heliyon* 10 (15) (2024) e35187.
- [97] X. Xu, P. Jiang, D. Liu, Y. Lyu, X. Shi, Z. Ji, X. Wang, 3D printable ionic conductive hydrogels with super stretch and self-adhesion performances for flexible sensors, *Giant* 17 (2024) 100237.
- [98] L. Wang, T. Xu, X. He, X. Zhang, Flexible, self-healable, adhesive and wearable hydrogel patch for colorimetric sweat detection, *J. Mater. Chem. C* 9 (41) (2021) 14938–14945.
- [99] J. Ren, M. Li, R. Li, X. Wang, Y. Li, W. Yang, Transparent, highly stretchable, adhesive, and sensitive ionic conductive hydrogel strain sensor for human motion monitoring, *Colloids Surf. A: Physicochem. Eng. Asp.* 652 (2022) 129795.
- [100] Kumar, A.; Jagannathan, N. J. p., *Cytokeratin: a review on current concepts.* 2018, 8, 10.
- [101] H. Niehues, J.A. Bouwstra, A. El Ghalbzouri, J.M. Brandner, P. Zeeuwen, E.H. van den Bogaard, 3D skin models for 3R research: the potential of 3D reconstructed skin models to study skin barrier function, *Exp. Dermatol.* 27 (5) (2018) 501–511.
- [102] A. Pariskar, P.K. Sharma, U.S. Murty, S. Banerjee, Effect of tartrazine as photoabsorber for improved printing resolution of 3D printed "Ghost Tablets": non-erodible inert matrices, *J. Pharm. Sci.* 112 (4) (2023) 1020–1031.
- [103] R. Chand, G. Janarthanan, K. Elkhoury, S. Vijayavenkataraman, Digital light processing 3D bioprinting of biomimetic corneal stroma equivalent using gelatin methacryloyl and oxidized carboxymethylcellulose interpenetrating network hydrogel, *Biofabrication* 17 (2) (2025).
- [104] S.G. Lee, K.J. Yu, S.M. Won, J.Y. Yoo, Advanced approaches to decoupled sensory signal monitoring in human interface systems, *Int. J. Extreme Manuf.* 7 (4) (2025) 042003.
- [105] K. Lee, O. Gul, Y. Kwon, J. Jeong, S. Cho, J. Ahn, J. Yu, C. Kim, D. Lee, H. Han, B. Lee, J. Choi, J. Ha, Y. Jeong, K. Kang, A. Javey, J. Ahn, I. Park, Smarter sensors through machine learning: historical insights and emerging trends across sensor technologies, *Adv. Funct. Mater.* (2025) e19859 n/am/a.
- [106] Z.M. Li, J.Y. Huang, R.H. Zhou, Z.Y. Chen, W.C. Gao, J. He, R.R. Bao, C.F. Pan, Temperature decoupling of a hydrogel-based strain sensor under a dynamic temperature field, *Adv. Mater. Technol.* 8 (17) (2023) 2300404.
- [107] R. Yang, W. Zhang, N. Tiwari, H. Yan, T. Li, H. Cheng, Multimodal sensors with decoupled sensing mechanisms, *Adv. Sci. (Weinh)* 9 (26) (2022) e2202470.